Chair of Cartography
Department of Civil, Geo and Environmental Engineering
Technical University of Munich

Master Thesis

Flood Mapping with the Sentinel-1 Time-Series Data in Arid Areas

Kamila Ćwik

Chair of Cartography
Department of Civil, Geo and Environmental Engineering
Technical University of Munich

Master Thesis

Flood Mapping with the Sentinel-1 Time-Series Data in Arid Areas

Author: Kamila Ćwik

Supervisor: M.Sc. Ekaterina Chuprikova

Dr. Corné van Elzakker

Dr. Sandro Martinis

Submission Date: Monday 23rd October, 2017

Matriculation number: 03670682

Place: München, Deutschland

Statement of Academic Integrity

I,
Last name: Ćwik
First name: Kamila
ID No.: 03670682

hereby confirm that the attached thesis,

Flood Mapping with the Sentinel-1 Time-Series Data in Arid Areas

was written independently by me without the use of any sources or aids beyond those cited, and all passages and ideas taken from other sources are indicated in the text and given the corresponding citation.
I confirm to respect the "Code of Conduct for Safeguarding Good Academic Practice and Procedures in Cases of Academic Misconduct at Technische Universität München, 2015", as can be read on the website of the Equal Opportunity Office of TUM.
Tools provided by the chair and its staff, such as models or programs, are also listed. These tools are property of the institute or of the individual staff member. I will not use them for any work beyond the attached thesis or make them available to third parties.

I agree to the further use of my work and its results (including programs produced and methods used) for research and instructional purposes.

I have not previously submitted this thesis for academic credit.

Munich, October, 23, 2017 _____

Declaration for the transfer of the thesis

I agree to the transfer of this thesis to:

- Students currently or in future writing their thesis at the chair:
  - ☐ Flat rate by employees
  - ☐ Only after particular prior consultation.
- Present or future employees at the chair
  - ☐ Flat rate by employees
  - ☐ Only after particular prior consultation.

My copyright and personal right of use remain unaffected.

Munich, October, 23, 2017 _____

Acknowledgement

I would like to offer great appreciation to my supervisor M.Sc. Ekaterina Chuprikova for the useful comments, remarks and engagement through the learning process of this master thesis. Furthermore, I would like to thank Dr. Sandro Martinis for introducing me to the topic and Dr. Corné van Elzakker for valuable guidance and the support on the way.

In addition, I would like to thank M.Sc. Eric Paul Jacobsen for writing assistance, language editing, and proofreading.

I would like to express my very profound gratitude to my loved ones for providing me with unfailing support and continuous encouragement throughout my years of study and through the process of researching and writing this thesis. This accomplishment would not have been possible without them. I will be grateful forever for your love. Thank you.

Contents

List of Figures

List of Tables

List of Abbreviations

AOI - Area of Interest
AWEI - Automated Water Extraction Index
DEM - Digital Elevation Model
DLR - German Aerospace Center
ESA - European Space Agency
GIS - Geographic Information System
LiDAR - Light Detection and Ranging
MNDWI - Modified Normalised Difference Water Index
MODIS - Moderate Resolution Imaging Spectroradiometer
NASA - National Aeronautics and Space Administration
NDWI - Normalised Difference Water Index
NDVI - Normalised Difference Vegetation Index
NIR - Near Infrared Band
SAR - Synthetic Aperture Radar
S-1FS - Sentinel-1 Flood Service
SWIR - Shortwave Infrared Band
TOPSAR - Terrain Observation with Progressive Scans SAR
USGS - United States Geological Survey

Abstract

Floods are a very serious and frequent disaster occurring in many parts of the world. Mapping of inundated regions is crucial for determining the flood extent, deployment of emergency response teams, and assessment of damages and casualties. This thesis investigates flood mapping using Sentinel-1 time-series data in arid areas. The presented method aims to improve the flood classification results from Sentinel-1 Flood Service which are based on a single SAR image analysis. Water detection performed in arid regions derived from one SAR dataset is challenging because the backscatter of water is similar to sandy regions, leading to overestimations of flood extent. The main objective of the thesis is an assessment of the influence of time series on flood classification accuracy. This goal is accomplished by executing experimental tests on different statistical parameters, frequency classes and durations of time-series data in the chosen areas of interest, which are in Somalia and Iraq. The results obtained from confusion matrices indicate enhancement in Overall Accuracy of ~5% and User's Accuracy of more than 24%. Such an effort aims to advance the use of Sentinel-1 time-series data for arid areas and pave the way towards rapid flood mapping to support emergency management authorities.

Keywords: Flood, Flood Mapping, Sentinel-1, Time Series, Arid Areas

1. Introduction

1.1. Problem Statement

Floods are one of the most common natural hazards worldwide. As can be seen in Fig. 1, the frequency of occurrence of floods is much higher than other disasters. In years 1995–2015, floods were estimated to represent 43% of all weather-related catastrophes, reaching more than 3,000 documented events. Their widespread existence and destruction drives scientists to investigate this phenomenon thoroughly (Berz et al., 2001, Schumann, 2015).

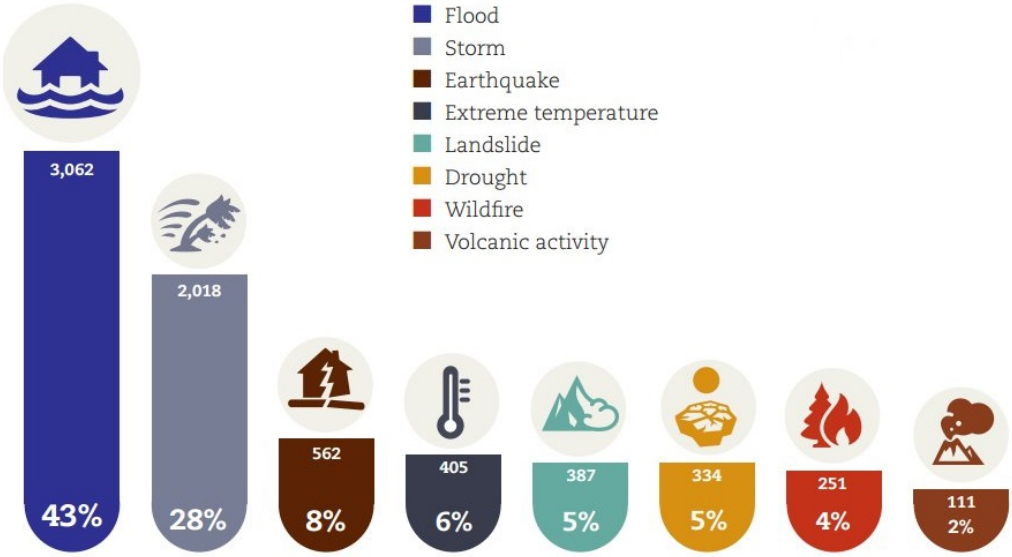

Fig. 1: Percentage of occurrences of natural disasters by disaster type in years 1995-2015 (UNISDR, CRED, 2016).

The first integration of remote sensing with flood monitoring mentioned in literature dates back to the 1970s, where data from Landsat 1 helped to analyze the Mississippi flood of 1973 (Deutsch and Ruggles, 1974). Since then, scientists have continued to use satellite data as auxiliary sources for multiple reasons, e.g., change detection, or observation of flood boundaries (Green et al., 2007, Moore and North, 1974). Remote sensing is widely used in all stages of disaster management (Fig. 2), from the mapping of flood-prone areas, through flood detection, early warning, evacuation planning, damage assessment and spatial planning (National Governor's Association, 1979). A variety of research techniques are being used, some based on passive remote sensing systems (Deutsch and Ruggles, 1974), some on active (Giustarini et al., 2015), and some combine both of them (Salvia et al., 2011, Tholey

et al., 1997).

In recent years Synthetic Aperture Radar (SAR), which is an active satellite system, gained importance mainly because of the all-weather, day-night acquisition

Fig. 2: The stages of disaster management (Marrion Consulting, 2016).

capability of its sensors (Mason et al., 2009), as well as due to the possibility of the detection of flooded vegetation (Horritt, 2003) and an ability to retrieve hydrological parameters, such as soil moisture (Tralli et al., 2005).

Sentinel-1 is a satellite mission of the European Space Agency (ESA) launched in April 2014. It regularly provides SAR data which are extensively used for various applications, e.g., observation of marine environments, sea-ice and oil spill detection, monitoring of urban areas, land surface motion risks and climate change, and mapping in support of humanitarian aid in crisis situations (Attema, 2005, ESA, 2012). The high quality data provided on an open and free basis are an attractive source of information for researchers.

1.2. Research Significance

Development of flood classification accuracy in arid areas is a significant issue that needs to be addressed. The aim of the technique described in this thesis is an enhancement of the results of the Sentinel-1 Flood Service. Sentinel-1 Flood Service is a web service that, based on a single SAR image, facilitates the generation of a flood mask (a map layer showing the extent of flooding) ready to be distributed to disaster management authorities. The limitation of SAR data in arid regions is an inability to differentiate between water and water-lookalikes (term from Martinis (2017)), which share similar low backscatter. This drawback negatively influences the classification results from Flood Service, resulting in overestimations of the water extent. The time-series method investigated in this thesis might help with overcoming those issues. Application of an exclusion layer (into the classification computed by Flood Service) derived from time-series based statistics can decrease overestimations in the water mask. This exclusion layer consists of areas with permanent low backscatter, which is related to regions continuously covered by sand. Implementation of this time-series based exclusion layer in the Sentinel-1 Flood Service can help to improve the classification accuracy. Improvements of this type also address initiatives related to rapid flood mapping, such as the International Charter "Space and Major Disasters".

Method based on time series was developed by a group of scientists in German Space Agency (DLR) and tested on one arid area (Martinis, 2017, Twele et al., 2016). This thesis aims to extend the experiments on that area using different time series durations, as well as testing several time series parameters. Furthermore, comparison between usage of time-series and MODIS as exclusion layer is performed. Additionally, other Area of Interest is chosen to establish if transferability of the method is possible.

1.3. Research Objectives

This thesis suggests a technique that could improve flood mapping in arid areas using Sentinel-1 time-series data. Until recently, arid regions were scarcely investigated due to difficulties with the interpretation of results (Martinis, 2017). This research will be guided by the following questions:

Research question 1:
Does the use of the Sentinel-1 time-series data improve flood mapping in arid areas in comparison to existing approach from Sentinel-1 Flood Service?

To answer the first question, floods that occurred in arid areas are studied. Information to help determine the timing and impact of these events comes from multiple, reliable sources. Second, visual confirmation is conducted by using optical data from Sentinel-2 and Landsat 8 data. Afterwards, time series of images from Sentinel-1 will be processed and merged into unique images representing different statistical parameters. This will be performed using an algorithm which is currently being developed by the Geo-Risks and Civil Security Department at the German Aerospace Center (DLR). Merging of an exclusion layer derived from time-series statistics and SAR-based flood classification from Sentinel-1 Flood Service is then carried out. The results from this process will be compared with ground-truth flood masks extracted from optical data by computation of confusion matrices.

Research question 2:
What is the influence of time-series parameters on classification accuracy?

High classification accuracy is often a goal for researchers. One of the objectives of this research is an improvement of the classification accuracy of flood mapping by using statistical parameters derived from time-series data. They are based on backscatter values categorized in ten frequency classes distributed from 0-100% (Martinis, 2017). Each class will be compared with the flood mask from Sentinel-1 Flood Service through calculation of confusion matrices. Performing confusion matrices on these multiple time-series parameters will help to determine their influence on the classification accuracy.

Research question 3:
What are the uncertainties and limitations of this approach?

Every technique of image processing carries some uncertainties and limitations. The approach described in this thesis will encounter them as well. Each step in the methodology will address this third research question. Aspects which might be expected to lead to uncertainties are as follows:

- long processing time,
- memory deficiency,

- lack of specific available data (e.g., validation), and
- influence of environment.

1.4. Thesis Outline

To investigate the objectives of the study, this thesis has the following structure. In Chapter II, background information such as the definition of flood and climate classification are discussed. Also, an outline of the state of the art is presented. Chapter III introduces the datasets used and chosen areas of interest. Chapter IV is devoted to the methodology adopted to perform the research. Experimental results are shown in Chapter V. The conclusions and recommendations are reported in Chapter VI.

2. Background and State of the Art

The previous chapter introduces the problem of flood classification accuracy in arid areas, which is tackled in this thesis. Significance to the field is underlined and research objectives are presented to show the aim of the study. This chapter introduces types of floods and climate classifications that are used. The second part of the chapter is dedicated to discussing the state of the art of flood mapping methods based on remote sensing techniques.

A flood, according to AMS (2017b), is "an accumulation of water over areas that normally are not submerged." It is a natural phenomenon which can cause fatalities and damage to the environment as well as to the economic development of a community. The increase (or decrease) in destruction caused by the inundation highly depends on the actions taken by local and global authorities (European Parliament, 2007). Flood management plays a crucial role here, especially with a focus on flood mapping, monitoring, forecasting, warning, and floodplain management (Hong et al., 2013).

Floods can be categorized according to the speed of the water, geography or cause of flooding. Below are descriptions of the most common types of floods (FLOODsite, 2009, NSSL, 2017, Wright, 2007):

- **River flood** - Takes place when water levels rise over the banks of the river. Generally, it is caused by high precipitation over extended periods of time; snow-melt and debris can worsen the overflow.

- **Urban flood** - Inundation of urban areas, when heavy rainfall exceeds the capacity of a sewer system and drainage canals. It can cause severe damage to infrastructure: roads can be blocked, water can get inside buildings through walls and floors or cause backup through toilets and sinks.

- **Coastal flood** - Inundation of regions along the coast, caused by the combination of high tides, increased precipitation and strong winds. The extent of this type of flood depends on topography, erosion conditions and the barriers on the coast (natural or man-made). **Storm surges**, generated by tropical and mid-latitude cyclones, are included in this group. Their severity depends on meteorological conditions, such as strong spiraling winds and low barometric pressure which cause an increase in the water level much higher than normal tide level. Damage can be very serious, especially given that coastal regions are usually major touristic and economic centers.

- **Flash flood** - A special type of flood because it can happen anywhere (e.g., on a river, in cities). It is caused by extremely intense precipitation within a short period and usually lasts only a few hours. The rapidity, ferocity, and intensity of the high water make this type of flood very dangerous.

2.1. Climate Classification

In this subchapter, climate classification and the definition of arid areas are presented. Many other classifications of the climate exist (Thornthwaite, Meigs), but for the purpose of this thesis, the classification of Köppen-Geiger is used. It was one of the first classifications of climates, introduced in 1900 by Wladimir Köppen, and later mapped by Rudolf Geiger in 1954 and 1961 (Köppen, 1900, 1918, Kottek et al., 2006). The climate categorization is based on the vegetation groups in a letter code designation (1 to 3 letters). The main division as follows :

- A - the equatorial zone,
- B - the arid zone,
- C - the warm temperature zone,
- D - the snow zone, and
- E - the polar zone.

Additionally, the following factors help with the specification of climates: the second letter refers to the precipitation amount and the third - to air temperature. In the case of areas described in this thesis, the focus is on BWh (Hot desert climate) and BWk (Cold desert climate), where B refers to arid climates, W to the desert, h to hot and k to cold (Fig. 3).

The criterion in Eq. 1 needs to be fulfilled to establish type B and Eq. 2 to establish type BW:

$$P_{ann} < 10\ P_{th} \tag{1}$$

$$P_{ann} \leqslant 5\ P_{th} \tag{2}$$

P_{ann} stands for accumulated annual precipitation [mm/year], and P_{th} denotes dryness threshold [mm].

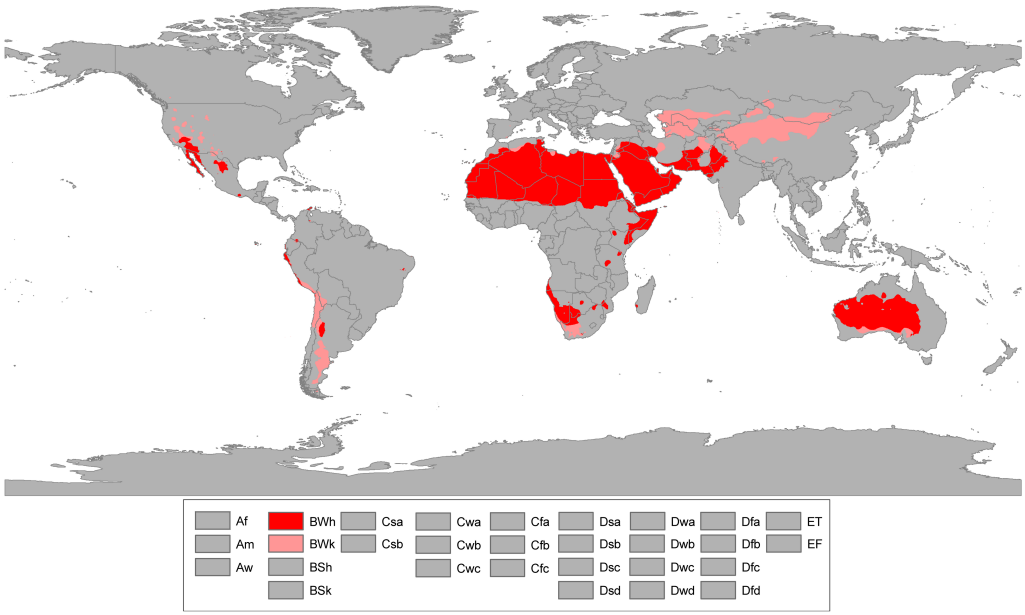

Fig. 3: Köppen-Geiger climate classification with focus on arid areas (Peel et al., 2011).

The following expression demonstrates how P_{th} is calculated:

$$P_{th} = \begin{cases} 2\{T_{ann}\} & \text{if at least 2/3 of the annual precipitation occurs in winter,} \\ 2\{T_{ann}\} + 28 & \text{if at least 2/3 of the annual precipitation occurs in summer,} \\ 2\{T_{ann}\} + 14 & \text{otherwise.} \end{cases} \tag{3}$$

P_{th} depends on the annual cycle of precipitation. $\{T_{ann}\}$ represents the absolute measure of the annual mean temperature [°C]. To specify climate as BWh, the criterion in expression needs to be fulfilled:

$$T_{ann} \geqslant +18\ ^{\circ}C \tag{4}$$

To determine climate as BWk, the principle in Eq. 5 has to be followed:

$$T_{ann} < +18\ ^{\circ}C \tag{5}$$

Due to specific atmospheric conditions, arid areas are characterized by a severe lack of water which prevents the development of vegetation (Oliver and Fairbridge, 1987). Those zones can be present in both hot and cold environments: at the equator, along coasts, on mountains and plateaus, at the poles, and below sea level.

2.2. Flood Mapping Using Remote Sensing Techniques

With the development of media and technology, information about floods has increased through the years. Many databases and initiatives have been created to provide knowledge to people about the dangers associated with floods: Emergency Disasters Data Base (EM-DAT), ReliefWeb, The Disaster Center, Associated Programme on Flood Management, WaterWatch, Global Flood Monitoring System (GFMS), International Flood Initiative, International Charter on Space and Major Disasters, PreventionWeb, Center for Satellite Based Crisis Information (ZKI), and many others (Hong et al., 2013). Similarly, many more studies involving mapping of floods and water surfaces were developed using remote sensing. They differ in their applied methods (index-based, thresholding, change detection), spatial resolution, the analysis approach (pixel-based, object-based), sensors used and, most importantly, by main data type - optical, SAR, Digital Elevation Model (DEM), Light Detection and Ranging (LiDAR).

2.2.1. Optical Data for Flood Mapping

Optical systems have been used for flood mapping since the 1970s (Deutsch and Ruggles, 1974). In 1996 McFeeters developed the Normalized Difference Water Index (NDWI). It is based on a comparison of the reflectances (ρ) of two spectral bands of the electromagnetic spectrum: green (G) and Near Infrared (NIR) (Eq. 6):

$$\begin{gathered} NDWI = \frac{\rho_G - \rho_{NIR}}{\rho_G + \rho_{NIR}} \\ NDWI \in -1, 1 \end{gathered} \tag{6}$$

where $NDWI > 0$ is a water class and $NDWI \leqslant 0$ - non-water. *The electromagnetic spectrum* is a sequence of all known frequencies of electromagnetic radiation. As can be seen in Fig. 4, the spectrum is described by wavelength [m] and frequency [s^{-1}] referring to one cycle per second, also called Hertz (Hz). If wavelength increases, then frequency decreases, e.g., gamma rays have a short wavelength but very high frequency (AMS, 2017a). Use of Eq. 6 leads to the delineation of open water features and their enhancement in the images, a desirable effect when analyzing flood mapping. The NDWI method has been used and modified by many scientists for their research, e.g., Rogers and Kearney (2004) used red and Shortwave Infrared Band (SWIR), Gao (1996) NIR and SWIR. Xu (2006) designed the Modified NDWI (MNDWI) index using the green spectral band and SWIR instead of NIR (Eq. 7),

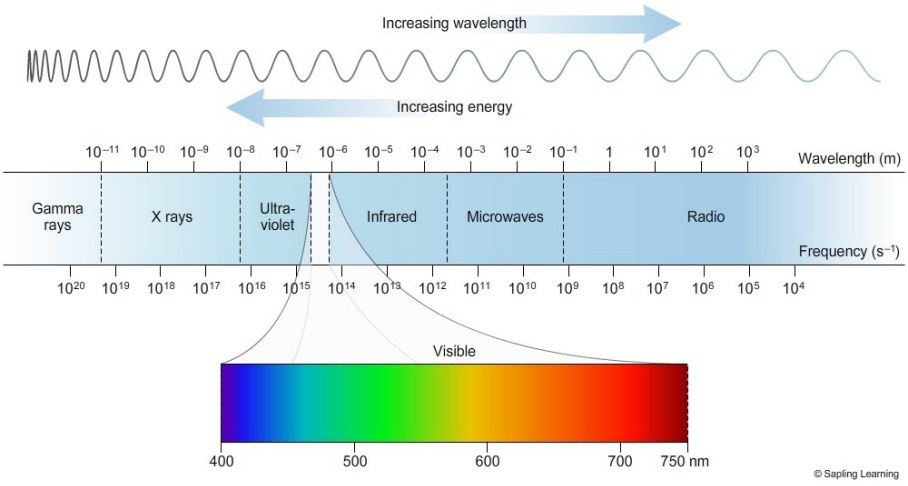

Fig. 4: Electromagnetic spectrum (Sapling Learning, 2017).

for improvement of the accuracy of water detection and omission of vegetation and soil noise.

$$MNDWI = \frac{\rho_G - \rho_{SWIR}}{\rho_G + \rho_{SWIR}} \tag{7}$$

MNDWI, similar to NDWI, has a threshold between classes equal to 0, but the method's author concluded that automation of the threshold value will lead to more accurate results. Ouma and Tateishi (2006) conducted tests with five different combinations of bands (including McFeeters' NDWI and Xu's MNDWI) and established that the best performance for detection of water bodies is when using $(SWIR - NIR)/(SWIR + NIR)$. Logically combining it with the Tasseled Cap Wetness index (compression of spectral data into a few bands) resulted in the creation of the Water Index.

The second method applied for optical data is single-band thresholding. *Thresholding* can be defined a method of image segmentation, which separates foreground from background using a pre-defined constant (Sezgin and Sankur, 2004). Baumann (1999) carried out tests to determine the spectral bands from Landsat TM that give the best results for identifying flooded areas. To find the desired band a density slicing approach was used, allowing separation of dry land surfaces, permanent water, and flooded areas. By analyzing the brightness histogram of the image, thresholds between classes were applied. Baumann concluded that NIR is the most suitable band for this approach. Frazier and Page (2000) used density slicing to determine classification accuracies of water boundary detection. The results were compared with maximum likelihood classification. This multiband supervised classification proved to be as efficient as density slicing method for detecting water bodies. Similar work was done by Jain et al. (2005). Nine spectral bands were examined, and the

conclusion was made that bands from the visible range with a uni-modal histogram show no distinct classes, whereas NIR has a clear bi-modal histogram. Although using the density slicing approach confirmed NIR as a suitable band for flood extent detection, better results were achieved with the NDWI method.

Another method used with optical data is linear unmixing, where the goal is segregation and clear class categorization of particular signals in a spectral composition. For example, Sethre et al. (2005) used a type of spectral unmixing called the Applied Analysis Spectral Analytical Process. This process differs from others because it does not require variety of spectral signatures, just from the class of interest.

The last group of methods can be categorized as thematic classification. Lira (2006) presented a methodology for segmentation of water bodies based on variation of principal component analysis, where training samples of water and land cover are collected and clustering of classes is performed. Another approach is presented by Hung and Wu (2005). By using a hierarchical unsupervised classification scheme, major land cover classes are distinguished: soil, wetland, water, developed and undeveloped land. This method is later used for change detection. The next example of thematic classification is presented in Li and Narayanan (2003), where a region growing algorithm was developed to collect training samples from different classes depending on particular spatial constraints.

It is very common practice to combine multiple methods of water extraction using optical imagery. Very often water indices are combined with thresholding and thematic classification with linear unmixing. Feyisa et al. (2014) merged the Automated Water Extraction Index (AWEI) with thresholding. To develop AWEI, a combination of 5 bands from Landsat 5 was used: blue, green, NIR and two bands from SWIR. This method offers improvement over other techniques because it correctly classifies regions that are covered by shadows. Sethre et al. (2005) joined linear unmixing with density slicing to achieve better results in delineation of water bodies. Furthermore, Sun et al. (2012) proposed two methods for extraction of water features. The first technique determines spectral reflectance curves for different water classes: clear, turbid and green. Results have shown that for clear water MNDWI is the most appropriate, for turbid water SWIR band and green water NIR. The second method is a combination of the first one and object-based image segmentation. The accuracy of the first method was higher, and one of the author's conclusions was to suggest future study about merging the first method with linear unmixing or other advanced classification algorithms. Jiang et al. (2012) integrated three spectral water indices: NDVI, MNDVI, NDBI (Normalized Difference Built-up Index) with HIS (Hue-Intensity-Saturation) transformation. This method is advan-

tageous for extraction of water bodies and exclusion of hill shadows, especially in complex terrain.

2.2.2. Data from Microwave Systems for Flood Mapping

Flood mapping can be based on passive and active microwave remote sensing (Fig. 5). The literature contains many examples of studies based on active or

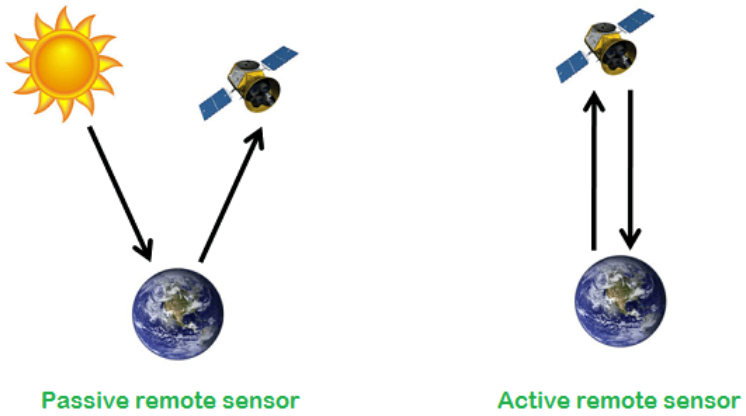

Fig. 5: Active and passive sensors (Physics and Radio Electronics, 2017).

passive sensors (sometimes also a combination of both), and some of them will be mentioned in this subchapter. Regardless of the source light for a specific satellite, each of them carries instruments which operate in different frequency bands. *Radar frequency bands* are defined as specified ranges of wavelengths in the microwave radiation portion of the electromagnetic spectrum (Table 1).

Table 1: Radar frequency bands (AMS, 2017c)

Frequency band	Frequency range (GHz)	Wavelength range (cm)
L band	1–2	15–30
S band	2–4	7.5–15
C band	4–8	3.75–7.5
X band	8–12	2.5–3.75
Ku band	12–18	1.67–2.5
K band	18–27	1.11–1.67
Ka band	27–40	0.75–1.11
V band	40–75	0.4–0.75
W band	75–110	0.27–0.4

According to IEEE-AESS (2003), letter designation serves several purposes:

- it is a convenient method for describing the band, without the need for specifics indicating numerical ranges,

- in the military, the exact frequencies of some operations cannot be revealed, but a general band description can be disclosed, and
- categorizing frequencies in bands helps with distinguishing their common characteristics, applications, and environmental constraints.

Passive Microwave Remote Sensing

The literature on flood mapping using passive microwave systems shows a variety of approaches. Passive sensors record electromagnetic radiation emitted from the surface of the Earth as well as reflected light from the sun (Fig. 5).

De Groeve (2010) presented a method based on passive microwave systems which can be used for the daily detection, mapping, and monitoring of floods. Quick identification of hazards is essential for decision makers and humanitarian organizations. Effective processing systems and the daily availability of data allow for the detection of floods in as little as 2 hours after their occurrence and for issuing early warnings based on monitoring of upstream areas. Although flood maps using passive microwave systems are low resolution, their accessibility supported a better understanding of dynamic processes occurring during flooding. Galantowicz (2002) proposed a prototype method of flood mapping based on low-resolution (20-70 km) passive sensors. A "flood-potential" database is built from historic flood images and used for development of high-resolution flood-extent maps. Future improvement and testing of this method is needed due to detected mapping errors.

Due to the low spatial resolution of the data from passive microwave remote sensing, greater focus is directed towards active systems.

Active Microwave Remote Sensing

Flood mapping using active microwave systems has been widely investigated. Active sensors possess their own source of electromagnetic energy, which is transmitted from the sensor towards Earth's surface. The signal reflected back to the satellite is called *backscatter*. Each material has a different reflectance, e.g., standing water has low backscatter, as it reflects most of the energy because of its smooth surface, where as vegetation, due to its rough surface, has high backscatter (ESA, 2013). There are some challenges involved when analyzing the received signal from flooded regions, such as *double-bounce scattering*, vegetation or atmospheric conditions. Double bounce most commonly occurs in flooded cities when a signal hits

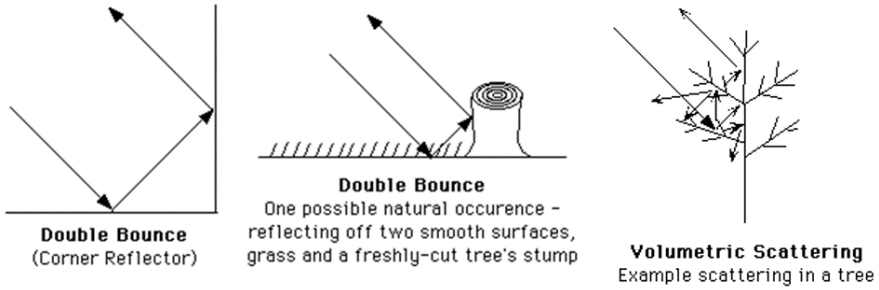

Fig. 6: Scattering of electromagnetic energy (ESA, 2014a).

water and is rerouted by nearby buildings' walls back to the satellite (Fig. 6). If the signal was not interrupted, the specular reflection of the smooth water surface would result in low values of backscatter in the image. Double bounce can take place in different areas, usually where vertical structures are present, such as forests. Trees can also cause a different type of scattering called *volumetric scattering* (Fig. 6), where the radiation is transmitted and refracted between many branches and leaves, causing interpretation of flooded vegetation to be very challenging. Atmospheric conditions such as wind can cause a smooth water surface to become uneven. In that situation if the sensors register the signal, it will lead to misinterpretations in analyzing the extent of water overflow. Scientists investigate those processes for better understanding and preparedness against floods.

Literature shows that sensors with particular spectral bands are used depending on the research focus. For example, L- and P-bands, as bands with longer wavelengths (Table 1), are more appropriate for detection of flooded vegetation, where C- and X-bands are more likely to be used for mapping open water and flooded areas with scarce vegetation (Brisco et al., 2008, Jensen, 2007).

A common technique for flood extent detection is the use of multi-temporal satellite images of the particular area and observing changes occurring during the chosen period. Often a combination of two images is used: one before the event and one during or shortly after the flood has occurred. When choosing the second image, it is important to be aware of which flood type is analyzed. If it is a flash flood, the image should be from the same day (flash floods can occur and be gone in 5-6 hours), but with longer standing water the time constraint is more flexible (can be a couple of days). An example of this method is presented in Brivio et al. (2010). In this work, images were analyzed one month before and three days after the event, when a flood was no longer at its peak. Confirmation of that could be seen in the results where only 20% of the actual flood extent was detected. To improve performance, an additional Geographic Information Systems (GIS) method was implemented. It is referred to as the least accumulative cost-distance matrix. It determined which

parts of the terrain (taking into account topography, vegetation cover, land flow and roughness) were least costly (least resistive to flow) for the river to flow over. The approach of integrating SAR and GIS greatly improved accuracy results to 96% and solved the problem of time constraints for data acquisition.

Recent research is focused on flood detection in challenging regions such as among vegetation. As an example Townsend (2010) tested the relationship between forest structure and detection of flood extent using C-band SAR data. Although L-band is recognized as superior for flood mapping of forests, this study tested C-band due to its sensitivity to inundation below tree canopies. Analyses were performed on images with different polarization from two satellites: RADARSAT and ERS-1. The results showed that flooded forest could be precisely mapped using RADARSAT. The second source did not perform well. It was concluded that the results depended largely on the basal areas and the height of tree trunks from the ground to the bottom of the canopy. Another study with a focus on vegetation was performed by Pulvirenti et al. (2013). This was based on image segmentation and fuzzy logic. Fuzzy logic allows an element to have a degree of membership for different classes, whereas in traditional logic an element can belong to only one class, or the other (Pulvirenti et al., 2011). This study reached the conclusion that knowledge about land cover is crucial for the accurate interpretation of backscatter signals. Typically, flooded regions are represented by low values, while inundated vegetation might result in high backscatter. Those enhancement values due to vegetation can be explained by the double-bounce scattering of a signal between tree trunks and the water surface.

In recent years several publications have appeared documenting a TerraSAR-X-based Flood Service based on fuzzy logic, which was later adapted to Sentinel-1 data (Martinis, 2017, Martinis et al., 2015, Twele et al., 2016). This technique is a fully automated processing chain created for near-real-time flood detection and monitoring. It is used in operational crisis mapping by the Center for Satellite based Crisis Information in DLR. TerraSAR-X is acquiring data non-systematically, and therefore the Flood Service has to be activated on-demand. In the case of Sentinel-1, data are routinely collected by satellite, and there is no need for manual tasking of data. Omitting this time-consuming step leads to a reduction in distribution time to less than 45 minutes of the data to disaster management authorities. Despite its successes, further tests have revealed that this classification method overestimates flooded areas due to water-lookalikes related to sand surfaces (Martinis, 2017). The goal of this thesis is to test this method and improvement of the flood classification results.

Giustarini et al. (2013) continued the methodology described in Martinis et al.

(2015) with a focus on urban areas. The risk that floods represent cannot be treated lightly, especially in urban areas. Man-made structures negatively influence accurate flood mapping, thus for several years great effort has been devoted to the study of flood mapping in urban regions. This study introduced a fully automated SAR-based flood extraction method that merged region growing, change detection and backscatter thresholding. Giustarini et al. (2013) concluded that although the technique has potential, there is also a need for further improvement, with focus on shadows in-between buildings and rooftops.

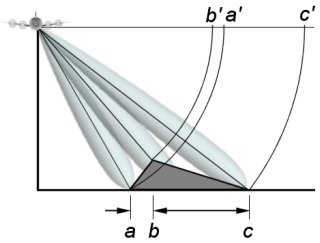

Fig. 7: Radar layover - before radar beam reaches the base of a tall feature (a), first it reaches the top of it (b) (Wolff, 2017).

An interesting approach for detection of urban flooding using double scattering was presented by Mason et al. (2014). Usually, double scattering (double bounce) positioned in radar layover (see Fig. 7) is considered a disadvantage of SAR as it distorts the length of electromagnetic waves, but this method tried to use its strengths. Test were made based on change detection cases and single-image analysis. The results demonstrated that detection of urban flooding is more effective with the use of double-bounce scattering.

The publication of Kiage et al. (2005) is an example of research performed for mapping of floods caused by other hazards. Hurricane Lili (2002) caused severe damage in the Caribbeans and in the south-east part of the United States, killing 15 people and causing damage worth about $925 million. Floods accompanying this hurricane occurred in Haiti, Jamaica, and in two states of the US: Mississippi and Louisiana (NHC, 2003). Kiage et al. (2005) performed tests to determine the usefulness of Radarsat-1 SAR imagery for flood detection by using arithmetic differencing and multi-temporal enhancement techniques. Vegetation and variations in elevation created certain obstacles in analyzing radar signatures from particular regions, but in general their method was successful in specifying the extent of flooded areas within coastal marshes.

The study in Chung et al. (2015) showed an example of a flood generated by a typhoon. It reached the northern part of Taiwan in July 2013, but the strength of this hazard affected Japan and China as well. Fatalities were estimated to be

as many as 11 killed, damage assessed at $557 million. A flash flood caused by extensive rainfall inundated areas of I-Lan County in Taiwan. Thanks to a good forecast, the COSMO-SkyMed satellite was directed at the affected area in time to collect data. As a result, a SAR-derived flood map was published within 24 hours of the event to support decision making authorities. This event later became the basis for developing standard operating procedures around the production of flood maps for future events.

2.2.3. Data Fusion for Flood Mapping

Many case studies are based on more than one data source. Mason et al. (2014) combined SAR data with LiDAR resulting in higher accuracy in the boundary between flooded and not flooded areas. The height information from LiDAR was used to generate a map of layovers and shadows and determine which of them were inundated. Mallinis et al. (2011) used radar and optical remote sensing for an approach that was aimed at accelerating the information dissemination process between neighboring countries, where weak bilateral cooperation reduces the efficiency of emergency management. Three object-based classification approaches were developed on multitemporal Landsat and Advanced SAR data, resulting in accurate flood maps that can be used for flood crisis management. Salvia et al. (2011) demonstrated a method of combining active microwaves (C-, X-, Ku- and Ka-bands) by utilizing an algorithm based on passive data, which assessed the fraction of the flooded area. Digital Elevation Model is a good source of auxiliary information, and it is often used to support flood mapping techniques. An example of this can be found in Brisco et al. (2008) and Pulvirenti et al. (2011), where DEM was implemented for better results. Schumann et al. (2011) used aerial photographic images with C-band SAR data. These methods focused on designing a model to represent the dynamics of floods in an urban environment.

2.3. Rapid Mapping of Floods

According to EMS (2015), *rapid mapping* is "fast, on-demand service delivery (within hours) of geospatial information in support of emergency management activities immediately following a catastrophic event. The service provision is based on rapid acquisition, processing, and analysis of satellite imagery and other geospatial raster and vector data." Irimescu et al. (2009) underlined the importance of

information derived from Remote Sensing and GIS techniques for disaster management authorities, decision makers, and relief personnel taking appropriate action at flooded sites. Maps of flood extent and risk zones are among the products that can be derived. Authors used a methodology based on Moderate Resolution Imaging Spectroradiometer (MODIS) data to estimate flood extent over particular land cover categories. MODIS data are available free of charge in near-real time but with 250 m spatial resolution and susceptibility to cloud coverage. The method was based on computing a Normalised Difference Vegetation Index (NDVI), which calculates the ratio between the NIR and red bands. NDVI is mostly used for vegetation monitoring, but Irimescu et al. (2009) demonstrated that water bodies can also be detected. Many publications have appeared in recent years demonstrating SAR to be a superior tool for flood mapping (Dumitru et al., 2015, Giustarini et al., 2015, Herrera-Cruz and Koudogbo, 2009, Martinis, 2017, Martinis et al., 2015, Martinis and Twele, 2010, Mason et al., 2014, Matgen et al., 2011, Pulvirenti et al., 2011, Twele et al., 2016).

Kwak et al. (2015) presented a method for rapid mapping of flooded rice fields. Risk maps are vital for near-real-time damage assessments, which influence the decisions made by disaster management personnel. Using multi-temporal data from MODIS and integration of a modified land surface water index (MLSWI), (Eq. 8) helped to assure information-rich assessment of flooded areas, including detection of the flooding start, peak, and extent. Additionally, a map of rice fields was created using MODIS land cover classification. The result of this method is to successfully provide instantaneous flood risk maps, which can be quickly distributed to emergency response teams in case of flooding.

$$MLSWI = \frac{1 - \rho_{NIR} - \rho_{SWIR}}{1 - \rho_{NIR} + \rho_{SWIR}} \tag{8}$$

Summary

This chapter provided definitions and overviews related to floods and the rapid mapping and description of flood types, as well as for relevant climate classification. A substantial part of the chapter covered State of the Art of current flood mapping techniques based on remote sensing. First, methods based on optical data were described. Following that was an overview of studies which use active and passive microwave remote sensing, with a concluding review of literature related to rapid mapping. The next chapter introduces the datasets used for testing the flood mapping method discussed in this thesis, and also presents chosen areas of interest.

3. Data and Study Area

The previous chapter introduced basic terminology related to arid areas and generation of floods, and presented previous initiatives and efforts in flood mapping and monitoring. It also presented the state of the art of flood mapping according to literature. This chapter will provide information about the datasets used to answer the research questions outlined in Chapter 1 of this thesis, and also describes the chosen Areas of Interest (AOI).

3.1. Datasets

Data products from Sentinel-1 and Sentinel-2 are freely available on the Copernicus Open Access Hub (`https://scihub.copernicus.eu/`). Registered users can choose the place, date and other required parameters and download the data. However, download speeds are limited to two datasets at a time per user.

Images from Landsat 8 are accessible from the United States Geological Survey (USGS) Earth Explorer (`https://earthexplorer.usgs.gov/`). Besides Landsat 8, other datasets are available on this server.

3.1.1. Sentinel-1

Sentinel-1 is a satellite mission developed by ESA under the Copernicus initiative (Fig. 8). It is a constellation of two satellites: Sentinel-1A launched on

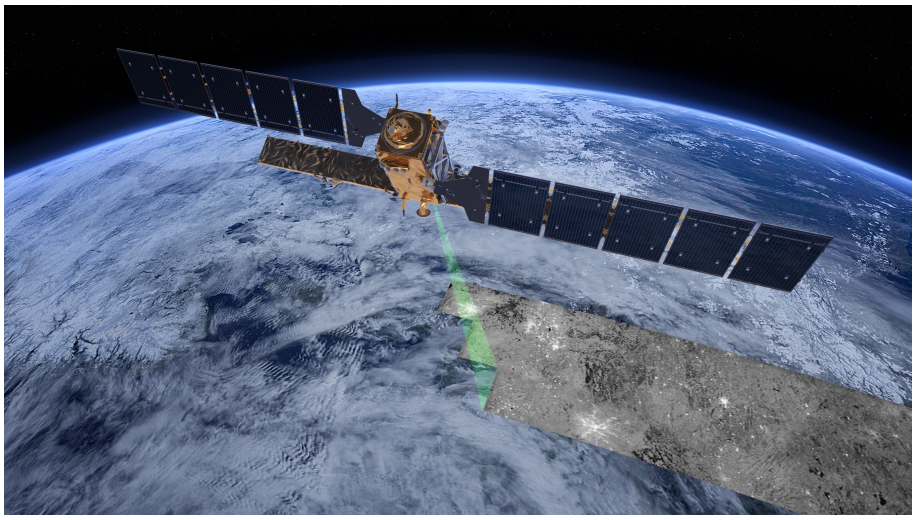

Fig. 8: Sentinel-1 radar vision (ESA, 2014b).

April 3rd, 2014 and Sentinel-1B launched on April 25th, 2016 (in the future two more units will be launched: Sentinel-1C and Sentinel-1D). Both satellites fly in the same sun-synchronous, near-polar, circular orbit at a height of 693 km, with a 12-day repeat cycle for one satellite, and 6-day for the pair (ESA, 2012, 2013). The SAR instrument operates in C-band, which is within the 4–8 GHz frequency range (7.5–3.75 cm wavelength), in the microwave portion of the electromagnetic spectrum (IEEE-AESS, 2003).

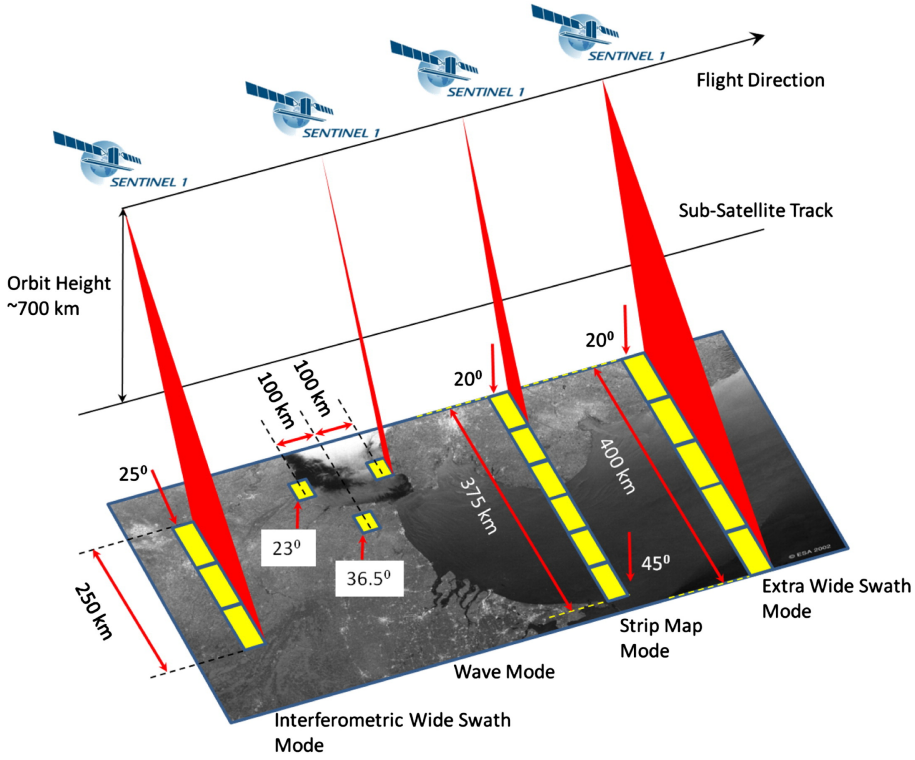

Fig. 9: Sentinel-1 acquisition modes (ESA, 2013).

Sentinel is used in a broad range of applications because of convenient access to its data and because it is free of charge. As can be seen in Fig. 9, data can be collected in four modes:

- **Stripmap mode (SM)** - collects data at 5 x 5 m spatial resolution with an 80 km swath width (the strip of surface captured by the satellite from which data are collected and later analyzed). SM is effectively a direct continuation of ERS and Envisat missions. The European Remote Sensing Satellite (ERS), launched in 1991, and Envisat in 2002 were two of the first Earth-observing satellite programs funded by ESA. Stripmap mode is used mainly to support disaster management activities.

- **Interferometric Wide Swath mode (IW)** - has a broader swath, reaching up to 250 km with 5 x 20 m spatial resolution. This mode uses Terrain Observation with Progressive Scans SAR (TOPSAR) to create higher quality data. This is the default acquisition mode over land.

- **Extra Wide Swath mode (EW)** - is mainly used for ice and oil spill monitoring, as well as for maritime and polar areas. It is suitable for those applications because of its wide swath coverage of over 400 km with 20 x 40 m spatial resolution.

- **Wave mode (WV)** - its acquisition path varies from the others. Instead of a continuous path, images called vignettes are collected in a "leapfrog" pattern. 20 x 20 m vignettes are acquired every 100 km at 5 x 5 m spatial resolution. This is the default acquisition mode over open ocean, often used for determining the wavelength, height, and direction of waves in the sea.

Wave mode is available in single polarization (VV or HH), SM, IW, and EW modes in single and dual polarization (VV+VH or HH+HV). For the purposes of this research, only the data products from IW mode are used.

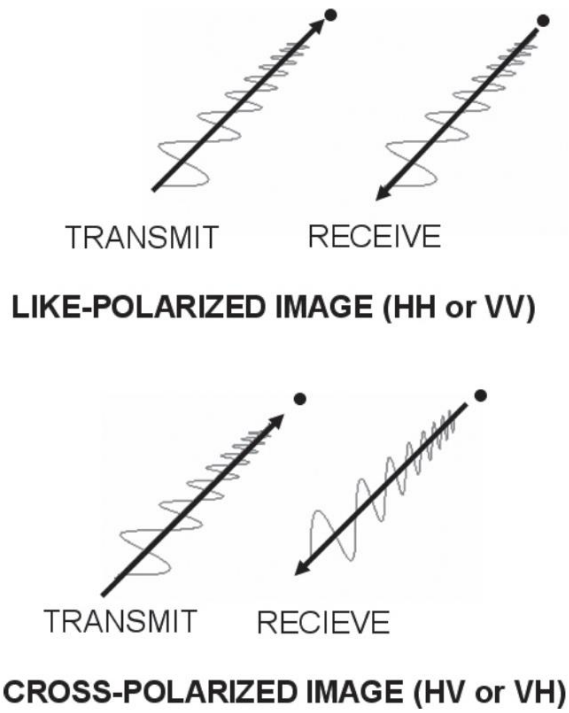

Fig. 10: Radar polarization modes (Campbell and Wynne, 2011).

As stated in Campbell and Wynne (2011) "the *polarization* of a radar signal denotes the orientation of the field of electromagnetic energy emitted and received by the antenna" (Fig. 10). The configuration of radar systems allows transmission and reception of horizontally (H) or vertically (V) polarized energy. If both transmission and reception are in the same direction, they are referred to as *like-polarized*. If they are perpendicular to each other, they are called *cross-polarized*.

Brisco et al. (2008) and Henry et al. (2006) analyzed the differences between HH, HV and VV polarization and they indicate that the best classification accuracies are obtained with HH. HV is shown to be worse than VV. Twele et al. (2016) investigated the classification accuracies for a test site using VV and VH, and the results suggest that VV is better. Although he admits that HH is superior for flood mapping purposes, he also underlines that this polarization has a low availability in Sentinel-1 data, and therefore the method focuses on VV polarization. Since this research is based on the technique described in Twele et al. (2016), the VV polarization is used.

3.1.2. Sentinel-2

Sentinel-2, similar to Sentinel-1, is a satellite mission developed under ESA's Copernicus initiative. It involves two satellites (Sentinel-2A and Sentinel-2B) on

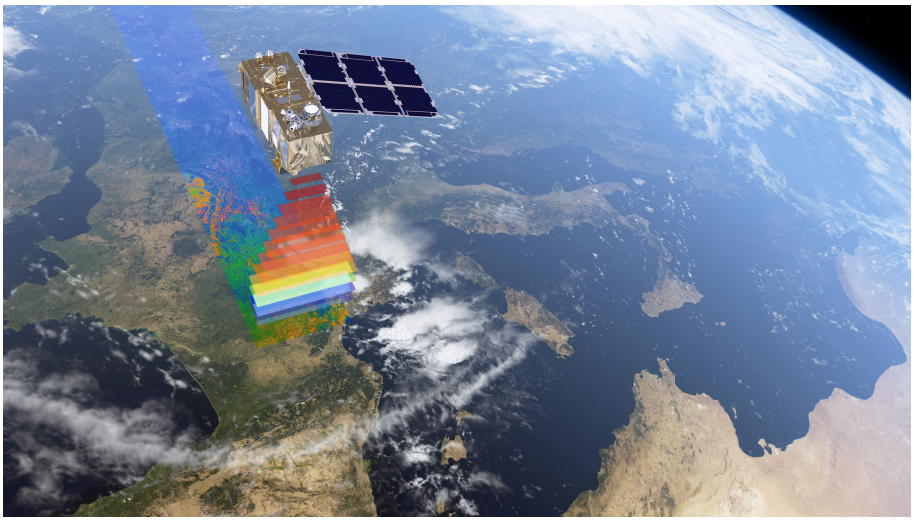

Fig. 11: Sentinel-2 satellite (ESA, 2015a).

opposite sides of sun-synchronous orbit at an altitude of 786 km (Fig. 11). Sentinel-2A was launched on June 23rd, 2015 and Sentinel-2B on March 7th, 2017. Each of them carries a Multispectral Instrument (MSI) collecting in 13 spectral bands at 10 m (4 bands), 20 m (6 bands) and 60 m spatial resolution (3 bands) (ESA, 2015b).

Sentinel-2 covers land and coastal areas from $56°S$ to $84°N$ with an orbital swath width equal to 290 km and a revisiting time of 10 days, or 5 for the pair. Sentinel-2 data can be used for such applications as water monitoring, forest and vegetation observation, as well as management of natural disasters and infrastructure, border, and maritime surveillance.

3.1.3. Landsat 8

Landsat 8, a result of a partnership between NASA (National Aeronautics and Space Administration) and USGS, is the most recent satellite from the Landsat program (Fig. 12). It was launched on 11^{th} February, 2013. Landsat instruments operate in X-band, within 8–12 GHz band (3.75–2.5 cm wavelength) of the electromagnetic spectrum (IEEE-AESS, 2003), on sun-synchronous orbit at a height of 705 km. It has a 16-day repetition, but together with its predecessor, Landsat 7, the combined Landsat repeat cycle is just 8 days (USGS, 2016).

Fig. 12: Landsat 8 satellite (NASA, 2014).

The Landsat 8 mission carries two instruments on board: an Operational Land Imager (OLI) and a Thermal Infrared Sensor (TIRS). OLI acquires data in 9 shortwave bands at spatial resolutions of both 30 m (8 bands) and 15 m (1 band). TIRS has two longwave thermal bands, both with 100 m resolution.

3.2. Data Availability

Satellite coverage is influenced by several factors, one of which is geographical coordinates. Close to the poles, the revisit frequency of a satellite is much higher than at the equator, e.g., Africa. To choose a potential area for this research, the images of a flood from Sentinel-1 have to be coordinated with Sentinel-2 or Landsat 8. The sensing period in both datasets should be, ideally, on the same day. That is problematic because floods often occur as a result of increased precipitation, and cloud coverage makes it difficult to use optical data such as Sentinel-2, and Landsat 8. Fig. 13 shows a Peru flood from March 2017 with low and high cloud coverage. The clouds in the right image prevent visual validation of the flood. This example shows why many potential AOI's have to be rejected, which causes testing of the transferability of the method described in this thesis to be very challenging.

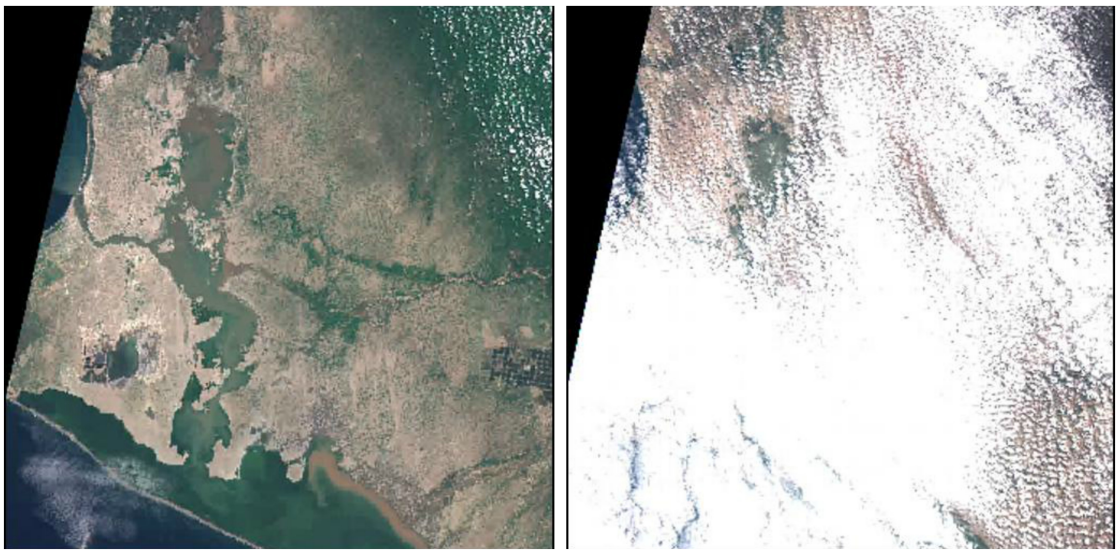

Fig. 13: Peru flood in March 2017 with low and high cloud coverage (Scihub, 2017).

3.3. Areas of Interest

The next subchapters describe the AOI's which are used to test Sentinel-1 time-series data for flood mapping in arid areas. A *Time Series* is a "sequence of data points evenly sampled through time" (Campbell and Wynne, 2011). The AOI's are chosen based on Köppen-Geiger's climate classification. Arid climates, both hot and cold, are taken into consideration. Regions that fulfill this requirement, as well as where a flood can be detected in the Sentinel-1 data, but which do not have visual validation from optical data are excluded.

3.3.1. Somalia

The first AOI is situated in Somalia, 11 km south of the city of Beledweyne (Fig. 14). It covers an area of 105 km^2, with the upper left corner at 4°41′43.58”N,

Fig. 14: Satellite view of AOI in Somalia (Google Earth, 2017).

45°17′17.31”E and the lower right at 4°35′36.39”N, 45°12′16.47”E.

Beledweyne is the fourth largest city (24 km^2) in Somalia with a population of 67,200, located 30 km south-east from the border with Ethiopia. In the last five years, temperature varied from 21 °C to 40 °C, with an average temperature of 33 °C (World Weather Online, 2017). During dry seasons the mean monthly precipitation is smaller than 10 mm of rainfall, and throughout wet seasons it does not exceed 70 mm (Climate-Data, 2017). The annual rainfall of this area is equal to 204 mm (Deutscher Wetterdienst, 2016). From its origin in Ethiopia, the Shabelle river flows south towards Mogadishu - the capital of Somalia. It runs through Beledweyne and the chosen AOI.

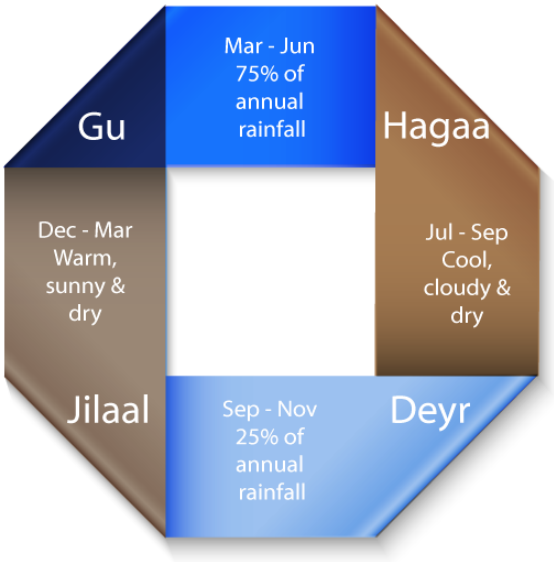

Fig. 15: Seasons of Somalia (FAO-SWALIM, 2017).

As can be seen in Fig. 15, the climate of Somalia can be divided into four distinct seasons with the main rainy season (Gu) spanning from late March to early June. As known from centuries of history, people living in areas with high temperatures and low precipitation would gather around rivers and water basins, due to fertile land and transportation possibilities. Similarly, in Somalia a high occurrence of droughts forced people to do the same; that is why farming regions are concentrated next to the rivers. According to the Central Bank of Somalia (2009), 80% of the population are pastoralists - breeders of livestock, especially camels, goats, sheep, and cattle, which also accumulate nearby reservoirs and rivers. Usually, the Shabelle River is perceived as a location of economic importance for agricultural reasons, but it is threatened by sudden floods that destroy crops, livestock, and homes, as well as contaminate fresh water, cause deaths, and generally affect thousands of people. In recent years the frequency and severity of this hazard has increased.

Historic events in the Deyr season (September-November) such as in 1961, 1977, 1997, 2006, 2012, 2014, and 2015 are examples of this, as well as crises which have occurred in the Gu season in 1981, 2005, 2013, 2016 (FloodList, 2017, Reliefweb, 2017, SWALIM, 2017).

Fig. 16: Destruction from the Somalia flood in May 2016 (FloodList, 2017, Red Cross, 2016, Shabelle Foundation, 2017).

Fig. 16 shows destruction caused by the flood of Shabelle in May 2016. This event started on May 15th and continued until the beginning of June. It affected more than 30,000 people, destroying crops and fields, and forcing tens of thousands of people to flee for higher grounds, leaving most of their belongings behind them. In such cases, the lack of safe drinking water and food, as well as spreading diseases, are very dangerous threats for a vulnerable population (FloodList, 2017). Prevention of such severe risks is a very import field of research. Planning emergency routes and assessing which areas are flood-prone are crucial. That is why flood mapping is essential information for decision makers and disaster management authorities.

3.3.2. Iraq

The second AOI is a region in Iraq. It covers an area of 3,974 km^2, with coordinates 33°1′38.35”N, 45°20′12.86”E (upper left) and 32°32′24.04”N, 46°7′23.03”E (lower right). The flood occurred 130 km south-east from Baghdad, 50 km from the western border of Iran (Fig. 17). This regions climate is classified as a Hot Desert

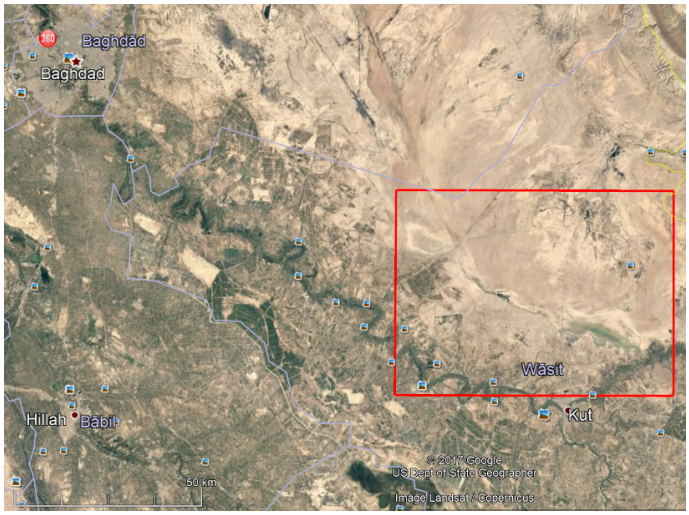

Fig. 17: Satellite view of AOI in Iraq (Google Earth, 2017).

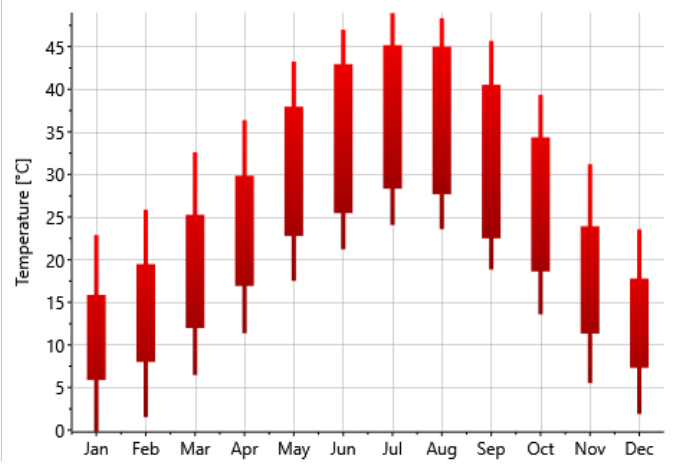

Fig. 18: Monthly average temperatures in Iraq (Remund et al., 2017).

climate with annual precipitation of about 120 mm and two weather seasons (FAO, 2011). The hot season spans from May to October with temperatures between 30–43° C and with heat waves to 48° C and higher. Winter season, from November to April, is colder, with temperatures ranging from 7-20° C (Fig. 18).

Heavy precipitation in late October 2015 caused severe flooding throughout

November. This led to the deaths of 58 people (mostly by electrocution) and displacement of more than 84,000 during an especially difficult crisis involving cholera outbreak. Another very serious effect of this flood was the displacement of landmines and other explosive remnants of war, which were transported by water to new unknown areas (FloodList, 2017, Reliefweb, 2015).

Fig. 19: Destructions of Iraq flood in November 2015 (AFP, 2015, Iraqi Red Crescent Society, 2015, OCHA/Linden, 2015).

Summary

This chapter presented the datasets necessary for performing time-series-based flood mapping. The products from Sentinel-1 used for creation of the time series are VV polarized in Interferometric Wide Swath mode. Optical data, such as from Sentinel-2 and Landsat 8 serve as reference data for the confusion matrices. Furthermore, study areas in Somalia and Iraq were described in detail. Information about the AOI climate, social aspects such as living conditions, and especially information about the studied floods such as the inundation levels and damage caused were provided.

4. Methodology

The previous chapter describes data sources which were used in this study and presents chosen test areas. The focus of this chapter is on the methods used. The methods workflow can be divided into two stages: choosing a potential flood (Fig. 20) and processing of the chosen Area of Interest (Fig. 21 - workflow adapted from Martinis (2017)). The first stage is focused on finding information about

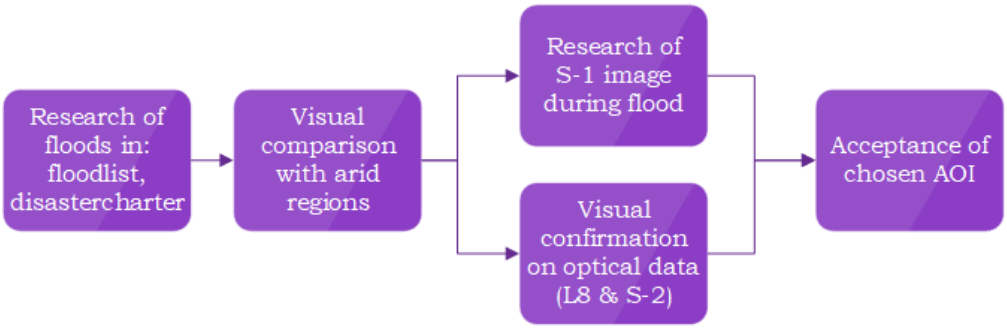

Fig. 20: Workflow of the first stage of research - choosing of possible flood.

historical floods with a focus on arid areas, visual detection of inundated terrain in Sentinel-2 and Landsat 8 data, as well as acquisition of a Sentinel-1 image during the event. This image is used in Sentinel-1 Flood Service to create a flood mask. This mask, depicting the extent of inundated areas, is often an overestimate of the true flooded area due to similar backscatter signal of water and water-lookalikes, such as sand. In order to decrease those overestimations, a time-series-based exclusion layer

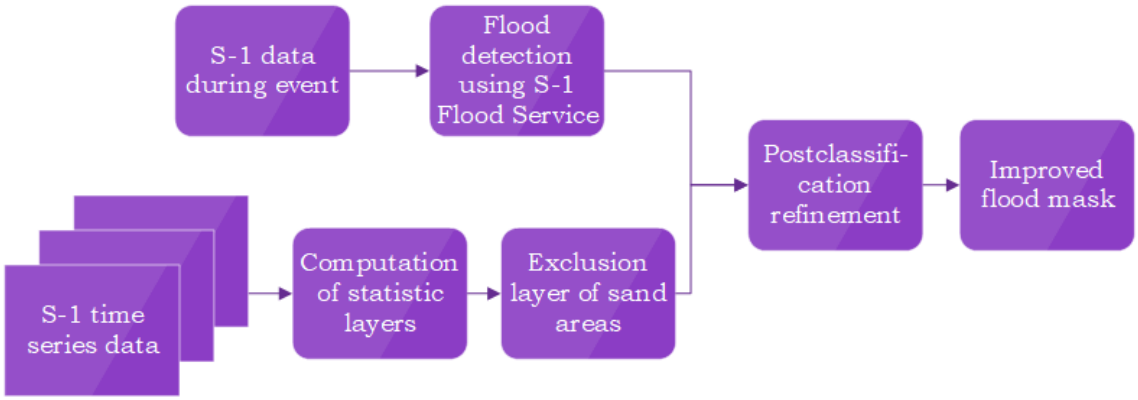

Fig. 21: Workflow of the second stage of research - processing of chosen AOI (Martinis, 2017).

designed to include areas with permanently low backscatter needs to be applied to the Sentinel-1 Flood Service flood mask. The exclusion layer is created from statistical parameters generated with a Python-based tool. To determine the best results from the different combination of parameters, several tests are performed.

4.1. Detecting a Potential Flood

The first step of the process is finding in available databases (`floodlist.com`, `disastercharter.org`, `emdat.be`, etc.) information about floods which occurred in the past. Since the Sentinel-1 satellite started collecting data in April 2014, the possible range of research starts from that time until the present.

The first factor to consider is the location. To qualify some event as a potential for further research, it has to be in an arid area (Fig. 3 from subchapter 2.1). That can be problematic because, to some extent, those databases rely on the media or word of mouth and information might not be precise. Also, the earlier a flood occurred, the fewer details can be found about the exact location. Fig. 22 shows

Flooding in Niger Leaves 12 Dead

15 AUGUST, 2014 BY RICHARD DAVIES IN AFRICA

Moroccan media are reporting that 12 people have been killed and nearly 30,000 affected by floods in Niger.

The information comes from a statement made on Thursday 14 August by the country's Humanitarian Coordination Unit of the Prime Minister. The statement also said that over 4,000 houses have been damaged in the recent flooding. Over 2,000 hectares of crops have also been damaged. Food and other relief supplies have only reached around half of the flood victims so far.

Heavy rain has affected areas of Niger for the last few days. Currently the worst affected areas are central and western regions, although the heavy rain is now spreading across other parts of the country. Mainé-Soroa in the south east saw 60 mm of rain fall in the last 24 hours.

Fig. 22: Example of a insufficient flood description (FloodList, 2017).

information that appeared on FloodList about an event in Niger on August 15th, 2014. The only indication of the flood extent is its description as occurring in "central and western regions [of Niger]". That information is insufficient to proceed with the research. This process is time consuming due to the need to confirm each of the articles separately for different countries and regions.

The next step consists of two simultaneous searches for:

- a single Sentinel-1 image,
- Sentinel-2 or Landsat 8 images.

Both searches should result in images that are very close in time, so that the extent of the flood has not changed over time.

4.1.1. Sentinel-1 Data

After precisely locating the flood, the overview of Sentinel-1 scenes can be started. To qualify an image as sufficient for the next steps, it has to be downloaded, calibrated and visualized. This is done in software called Erdas Imagine. After visual confirmation of the flood extent (and finding suitable optical data), the original image is processed in Sentinel-1 Flood Service (see subchapter 4.2).

4.1.2. Sentinel-2 / Landsat 8 Data

The optical data have to be coordinated spatially and temporary with the Sentinel-1 image. Here, atmospheric conditions play a critical role for visual confirmation of a flood (see Fig. 13 in subchapter 3.2). Afterwards, one or more images are downloaded and processed in Erdas (for classification) and ArcGIS software (for confusion matrices).

If those steps are achieved, the coordinates of the AOI have to be specified. They will be required for the time-series statistics. Later, the AOI can be accepted for testing with the method described in next subchapters.

Classification of optical data

The optical data from Sentinel-2 or Landsat 8 have to be prepared before they can be used for accuracy validation. The software Erdas Imagine is used for this purpose. First, stacking of spectral bands is performed with a tool called layer stack. Next, a water mask is made using a build-in NDVI unsupervised classification tool (Fig. 23). To determine which band combination could achieve the best classification results, tests were performed in comparison with visual interpretation. These tests lead to the conclusion that Xu's NDWI should be used (Eq. 7):

$$MNDWI = \frac{\rho_G - \rho_{SWIR}}{\rho_G + \rho_{SWIR}} \qquad \text{(7 revisited)}$$

The the output of this algorithm is a raster with binary values, where 1 is water and background is 0. Manual correction is applied in order to delete standing water (river, lakes) from the classification. This reference mask is later utilized in the confusion matrix (subchapter 4.4).

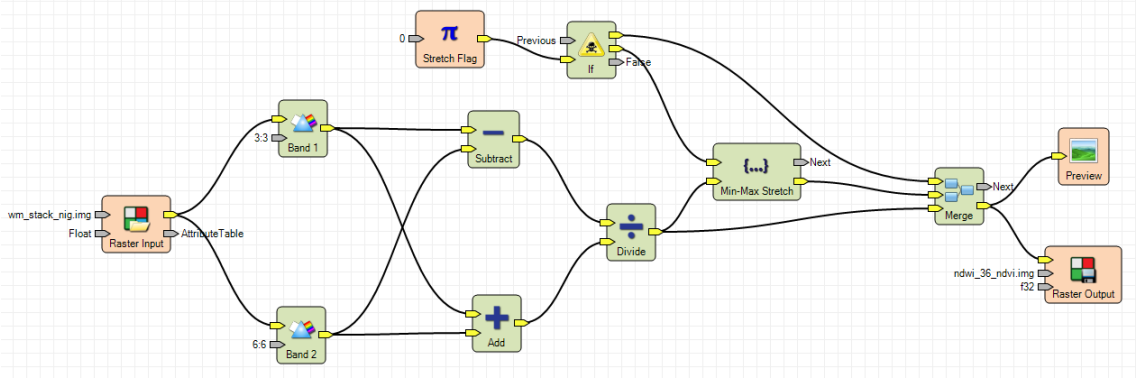

Fig. 23: Model of NDWI index.

4.2. Flood Classification / Sentinel-1 Flood Service

This subchapter presents a method of extracting flood classification results from Sentinel-1 Flood Service (S-1FS). A Sentinel-1 image with confirmed flood extent is processed in S-1FS. The processing chain is composed of following elements (Twele et al., 2016):

- **automatic data ingestion** - data in IW mode are consistently acquired and downloaded when matching the user request,
- **geometric correction and radiometric calibration** - implementation of auxiliary tools and datasets: graph processing tool from Sentinel Application Platform (SNAP) and DEM from Shuttle Radar Topography Mission (SRTM),
- **automatic thresholding** - tile-based thresholding based on (Martinis et al., 2009) procedure for generation of land/water classification,
- **fuzzy logic-based refinement** - improving the accuracy by eliminating probable water-lookalikes from initial classification using fuzzy logic,
- **final classification** - additional accuracy enhancements by using: Height Above Nearest Drainage (HAND) Index to establish flood-prone areas, SRTM Water Body Data and MODIS to distinguish and separate permanent water bodies,
- **data dissemination** - three layers are distributed through geoserver: flood water, standing water, and non-water.

A flood water mask produced from S-1FS is used for the next steps. Overestimations are reduced by applying an exclusion layer generated from Sentinel-1 time series

(described in section 4.4).

4.3. Creation of Time Series Statistics

This subchapter describes the usage of an existing Python-based tool, created to perform calibration and merging of the Sentinel-1 datasets, as well as computation of time-series statistics.

Firstly, a duration period for the time series is established with consideration of the balance between computation time and desired accuracy of classification results. The Python-based tool downloads all available data for the period and within the geographical coordinates chosen by the user. Afterwards, the geometric correction and radiometric calibration are executed. Later, frequency maps are created (with dB as a unit) that count how many times (throughout the whole time series) each pixel is detected with backscatter value below threshold τ. If a pixel is detected with high frequency, it means that most (or even all) of the time the area has low backscatter. That is related to standing water and water-lookalikes such as sandy regions, and should be excluded from classification. The frequency of pixels is scaled to a range 0-100% for interpretation purposes (10 classes with 10% interval). Pixels with high frequencies are used to create an exclusion layer, which is used to improve the water mask from S-1FS.

An original image from Sentinel-1 is presented in Fig. 24a. The dark pixels represent areas with low backscatter, such as water or sand. When this image is processed in S-1FS, the resulting flood mask includes overestimations (Fig. 24b). Fig. 24c shows the exclusion layer, generated from the Sentinel-1 time series, which is chosen based on experimental results described in chapter 5. Applying this layer to the S-1FS flood mask leads to improved accuracy of the Flood Service.

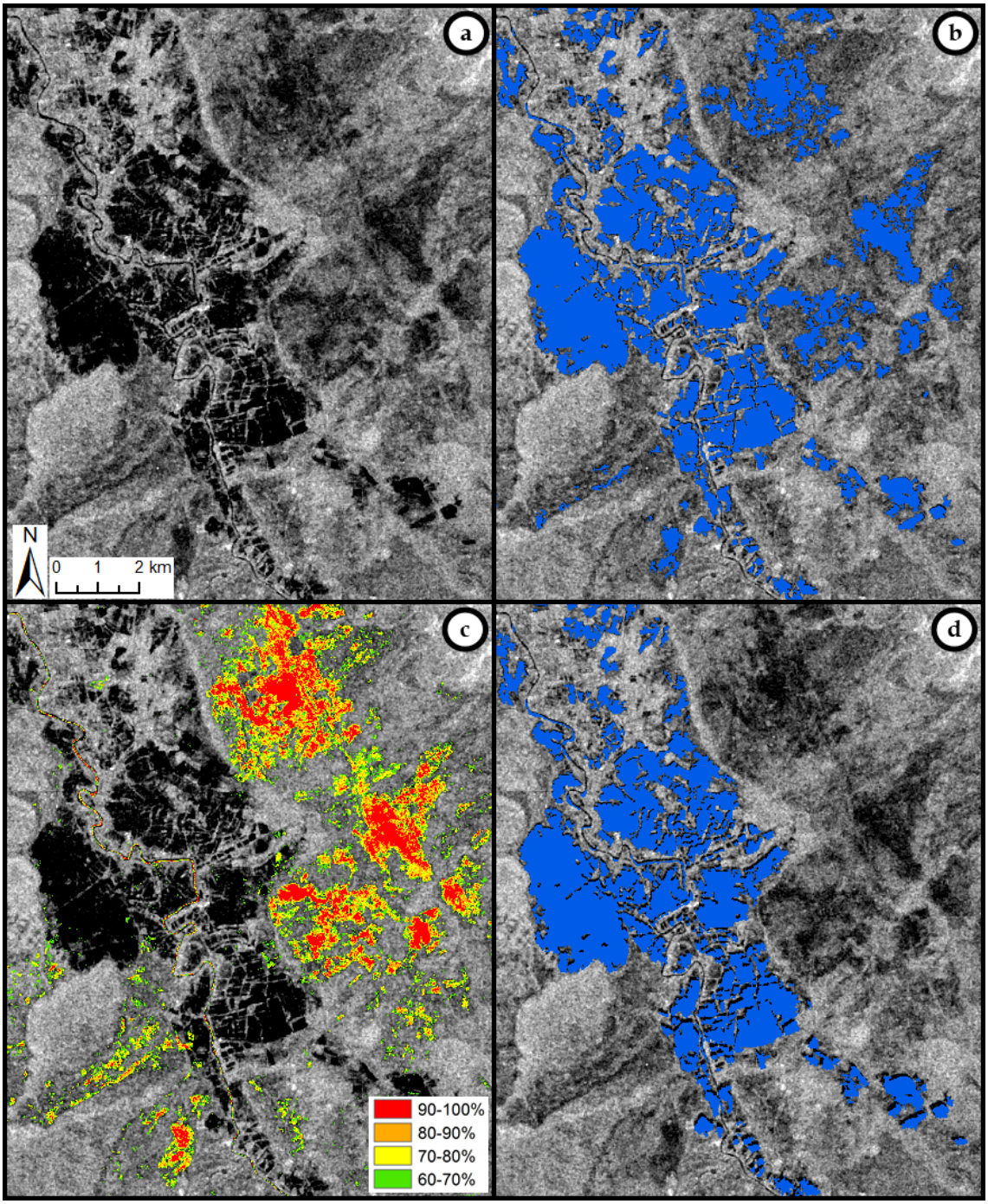

Fig. 24: Results from the process of improving accuracy: a) original Sentinel-1 image, b) overestimated flood mask from S-1FS, c) exclusion layer derived from time series, d) improved flood mask. See Fig. 14 for the location of the test site.

4.4. Postclassification Refinement

This step is designed for *accuracy assessment*. It is a comparison made between two sources of information: the map (analysis of remotely sensed data) and the reference data. If the research is time-sensitive, it is crucial to have time-correlated sources. To perform valid observations, the data have to be in the same geographical coordinate system with the same spatial extent, share the same minimum mapping unit, as well as number and meaning of categories (Campbell and Wynne, 2011).

The exclusion layer is created from a range of frequency classes chosen based on the experimental results from a confusion matrix.

The confusion (error) matrix shows a number of correct and incorrect predictions by comparing two data sources, which in this case are a reference mask from optical data (Sentinel-2 and Landsat 8) and an S-1FS flood mask improved using the exclusion layer. Compilation of this matrix is a necessity for most studies with a focus on accuracy improvement (Campbell and Wynne, 2011). For this research, the

Table 2: Confusion matrix

Result (x - 100%)		Reference Data		Row total
		Flood	Non Flood	
Classification Data	Flood	f/f	nf/f	UA1 = f/f + nf/f
	Non Flood	f/nf	nf/nf	UA2 = f/nf + nf/nf
Column total		PA1 = f/f + f/nf	PA2 = nf/f + nf/nf	**SUM = PA1 + PA2**

matrix consists of a 2x2 array, where the left side (y-axis) lists two map categories as determined from classification results (Flood/Non-Flood), and the upper labels (x-axis) show the same categories as determined from reference data (Table 2).

The first step to creating a confusion matrix is to perform raster calculation between the (overestimated) water mask from S-1FS and the frequency class from time series. Extraction of areas with permanently low backscatter improves the water mask, but the testing of different frequency classes has to be conducted to establish which classes give the best accuracy. By calculating the Overall Accuracy, User's Accuracy and Producer's Accuracy of different scenarios, determination of the best result can be achieved (Campbell and Wynne, 2011).

Overall Accuracy (OA) - total number of correctly classified pixels (diagonal elements) divided by the total number of all pixels (Eq. 9):

$$OA = \frac{f/f + nf/nf}{SUM} \tag{9}$$

Producer's Accuracy (PA) - an accuracy computed by analyzing the number of correctly classified pixels of a class and comparing it with all pixels of that ground truth class (Eq. 10):

$$PA = \frac{f/f}{PA1} \tag{10}$$

User's Accuracy (UA) - an accuracy calculated by investigating the number of correctly identified pixels in a given map class and comparing it with all pixels in this class in the classified image (Eq. 11):

$$UA = \frac{f/f}{UA1} \tag{11}$$

Summary

This chapter has outlined the methodology used in this masters thesis. It introduced the steps taken for detecting a flood, creation of a flood mask from reference data and also an exclusion layer based on time series statistics. It also provided an example of improvement in classification accuracy. Next, Chapter 5 will present the results obtained through the previously described methods.

5. Results

In flood mapping, the balance between accuracy and computing time is crucial, especially when the results have to be distributed in near-real time for disaster management authorities. This challenge motivated several experiments using the time-series approach outlined in Chapter 4. The usefulness of the proposed method for improving classification results from the Sentinel-1 Flood Service is assessed. The influence of different time-series parameters and the duration of the time series on classification accuracy is determined. This chapter describe the results from test sites in Somalia (5.1) and Iraq (5.2).

5.1. Somalia

This subchapter is divided into parts: 5.1.1 presents results from the time series spanning 2014–2017, 5.1.2 from the time series in 2015 and 5.1.3 from 2016. Each of them are analyzed to determine which period and parameter of time series are the most advantageous for future research. The last part of this subchapter (5.1.4) is devoted to a comparison of time-series period accuracies with results derived from MODIS data.

5.1.1. Time Series 2014-2017

The period of the first time series is from April 1st, 2014 to June 7th, 2017. In this time Sentinel-1 flew and captured images over the test site in Somalia 200 times: 13 images in 2014, 55 in 2015, 64 in 2016 and 68 in 2017. Fig. 25 shows the area of interest with multiple frequency class layers generated from the Python-based tool for calculating time series statistics. Each frequency class range is used in image calculation with an initial, uncorrected flood mask (with overestimates of flooding) from S-1FS. The resulting layer is analyzed using a confusion matrix with a reference flood mask derived from optical data. Based on Producer's and User's Accuracies, the frequency class with the best performance is used to create a sand exclusion layer. In Fig. 25 the image on the left depicts pixels with threshold frequency $\tau = -10$ dB (with colors used to indicate different frequency classes). The middle and right image, images have thresholds equaling –15 dB and –20 dB, respectively.

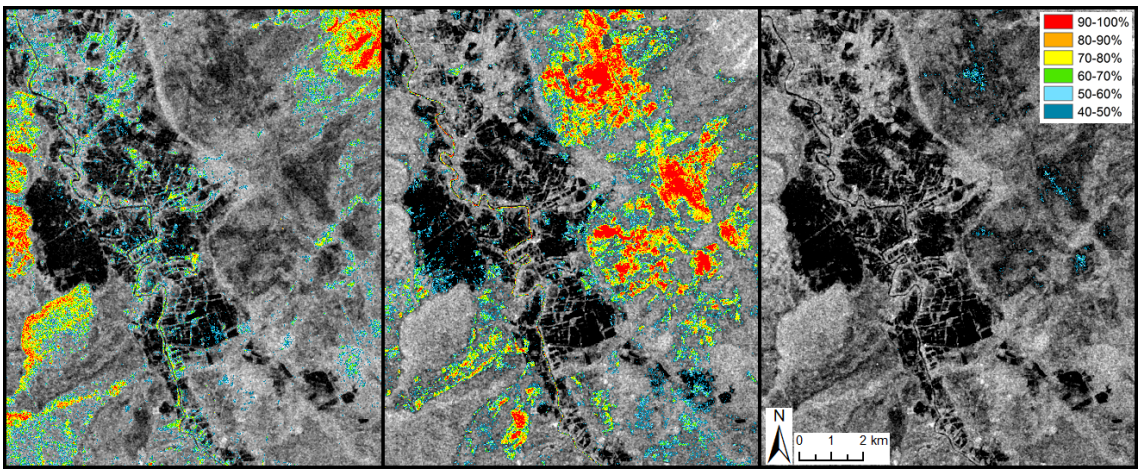

Fig. 25: Frequency classes in the study area in Somalia with τ equal –10 dB, –15 dB and –20 dB (left to right), with the Sentinel-1 image as background (2014–2017).

Frequency –10 dB

Table 3 displays both the matrix from the original image before application of the time series correction layer (Result 1), as well as the confusion matrices for the tested classes (Results 2-7) for a backscatter frequency of –10 dB. The numbers in the cells represent the number of pixels in the AOI which were identified for the respective classification. They are derived from image calculations in ArcGIS software.

Table 3: Confusion matrices for $\tau = -10$ dB (2014–2017)

Result 1 (Original mask)		Reference Data		Row total
		Flood	Non Flood	
Classification Data	Flood	142921	59806	202727
	Non Flood	5568	833255	838823
Column total		148489	893061	**1041550**

Result 2 (40-100%)		Reference Data		Row total
		Flood	Non Flood	
Classification Data	Flood	137383	59313	196696
	Non Flood	11106	833748	844854
Column total		148489	893061	**1041550**

Result 3 (50-100%)		Reference Data		Row total
		Flood	Non Flood	
Classification Data	Flood	141418	59605	201023
	Non Flood	7071	833456	840527
Column total		148489	893061	**1041550**

Result 4 (60-100%)		Reference Data		Row total
		Flood	Non Flood	
Classification Data	Flood	142748	59765	202513
	Non Flood	5741	833296	839037
Column total		148489	893061	**1041550**

Result 5 (70-100%)		Reference Data		Row total
		Flood	Non Flood	
Classification Data	Flood	142910	59801	202711
	Non Flood	5579	833260	838839
Column total		148489	893061	**1041550**

Result 6 (80-100%)		Reference Data		Row total
		Flood	Non Flood	
Classification Data	Flood	142921	59806	202727
	Non Flood	5568	833255	838823
Column total		148489	893061	**1041550**

Result 7 (90-100%)		Reference Data		Row total
		Flood	Non Flood	
Classification Data	Flood	142921	59806	202727
	Non Flood	5568	833255	838823
Column total		148489	893061	**1041550**

Table 4: Comparison of all accuracy results for $\tau = -10$ dB (2014–2017)

		Result 1 (S-1FS)	Result 2 (40-100%)	Result 3 (50-100%)	Result 4 (60-100%)	Result 5 (70-100%)	Result 6 (80-100%)	Result 7 (90-100%)
OA		93.7	93.2	93.6	93.7	93.7	93.7	93.7
PA	Flood	96.3	92.5	95.2	96.1	96.2	96.3	96.3
	non Flood	93.3	93.4	93.3	93.3	93.3	93.3	93.3
UA	Flood	70.5	69.8	70.3	70.5	70.5	70.5	70.5
	non Flood	99.3	98.7	99.2	99.3	99.3	99.3	99.3

The results are used to calculate the Overall, Producer and User's Accuracy (Table 4). It can be seen that a threshold of –10 dB is not suitable for this data. Result 1 (the original image from S1-FS) obtains the highest accuracy - only the 80% and 90% classes (Result 6 and 7) reach the same values, proving that this parameter is not adequate for an improvement to the S-1FS flood mask. Visual representation of those results can be seen in Fig. 26.

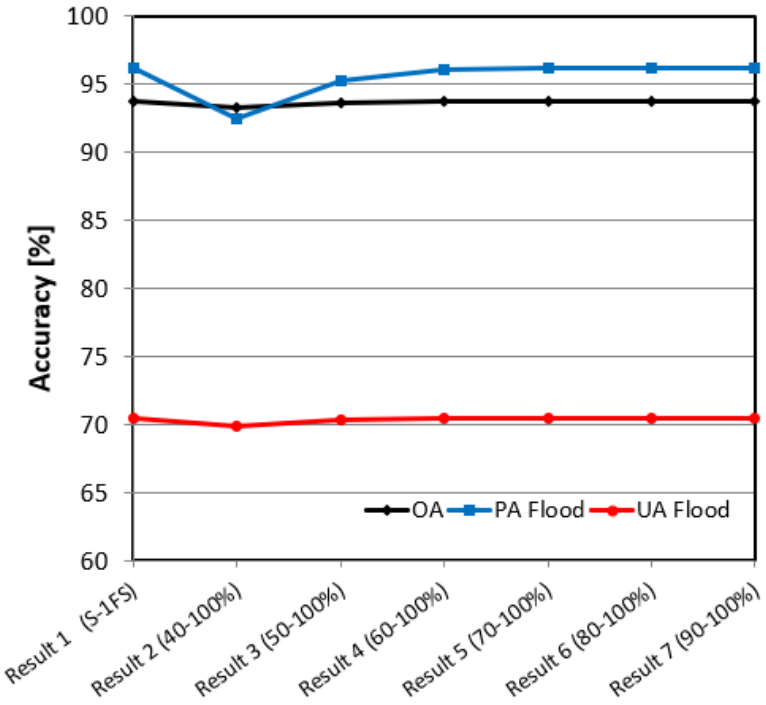

Fig. 26: Plot with accuracies of frequency classes with $\tau = -10$ dB (2014–2017).

Frequency –15 dB

The method used for analyzing threshold $\tau = -10$ dB is repeated for images with other backscatter thresholds. The detailed table with all of the confusion matrix results (as Table 3 for parameter $\tau = -10$ dB) can be found in Appendix B (Table 19). From Table 5 it can be seen that the best flood mask is achieved by the using

Table 5: Comparison of all accuracy results for $\tau = -15$ dB (2014–2017)

		Result 1 (S-1FS)	Result 2 (40-100%)	Result 3 (50-100%)	Result 4 (60-100%)	Result 5 (70-100%)	Result 6 (80-100%)	Result 7 (90-100%)
OA		93.7	97.3	98.0	98.4	98.3	97.9	96.4
PA	Flood	96.3	84.8	90.3	93.7	95.0	95.5	96.0
	non Flood	93.3	99.4	99.3	99.1	98.8	98.3	96.5
UA	Flood	70.5	95.8	95.5	94.7	93.1	90.4	81.9
	non Flood	99.3	97.5	98.4	99.0	99.2	99.3	99.3

frequency range 60-100% (Result 4) as the exclusion layer. Producer's Accuracy decreases from 96.3% by 2.5%, which means that slightly less of the actual flood (93.7%) was correctly classified as "flood" by the algorithm. The User's Accuracy, however, improves from 70.5% to 94.7%. This enhancement of 24.2% suggests that the flood classifications in the final result can be more reliably trusted, since 94.7% of flood classifications reflect ground truth. The general improvement from using this threshold is reflected by an Overall Accuracy value of 98.4%, up 4.7% from the original S-1FS. These are very promising results, particularly the significantly

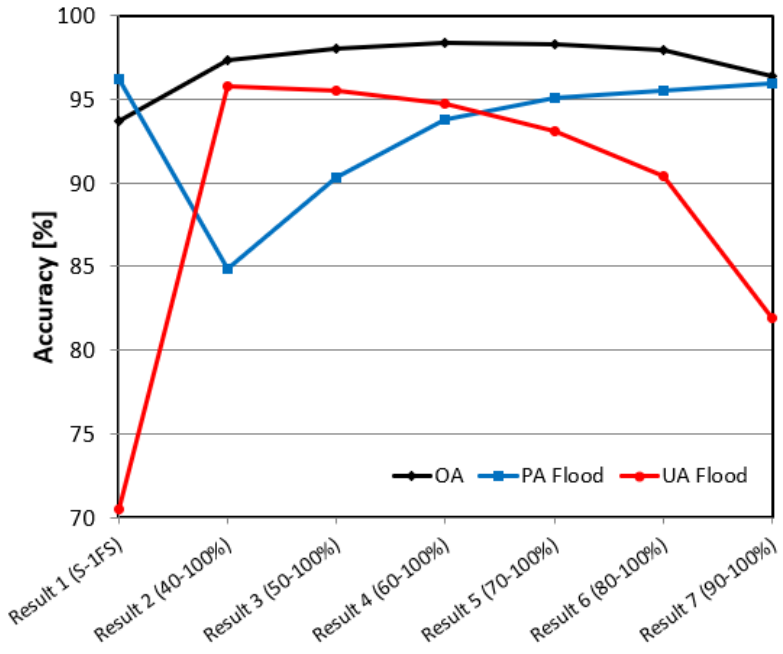

Fig. 27: Plot with accuracies of frequency classes with $\tau = -15$ dB (2014–2017).

increased reliability of classified flood pixels for end users. Fig. 27 represents the exclusion layers effects on accuracy results.

Frequency –20 dB

Table 6 illustrates accuracy results for $\tau = -20$ dB. For this threshold, the 40-100% frequency class (Result 2) slightly enhances the results. OA increases only 0.4%, PA drops 0.1%, and UA increases from 70.5% to 71.8%. This parameter is therefore not beneficial to accuracy improvement, as figure 28 shows visually. The full set of tables with confusion matrices is placed in Appendix B (Table 20).

Table 6: Comparison of all accuracy results for $\tau = -20$ dB (2014–2017)

		Result 1 (S-1FS)	Result 2 (40-100%)	Result 3 (50-100%)	Result 4 (60-100%)	Result 5 (70-100%)	Result 6 (80-100%)	Result 7 (90-100%)
OA		93.7	94.1	93.8	93.7	93.7	93.7	93.7
PA	Flood	96.3	96.2	96.3	96.3	96.3	96.3	96.3
	non Flood	93.3	93.7	93.4	93.3	93.3	93.3	93.3
UA	Flood	70.5	71.8	70.9	70.5	70.5	70.5	70.5
	non Flood	99.3	99.3	99.3	99.3	99.3	99.3	99.3

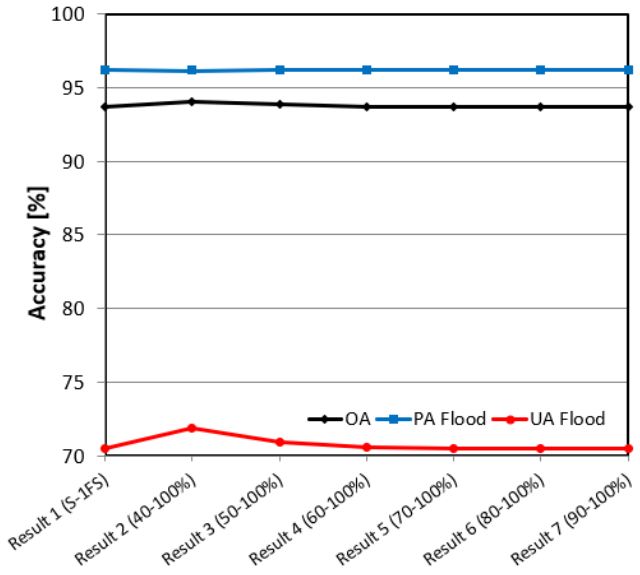

Fig. 28: Plot with accuracies of frequency classes with $\tau = -20$ dB (2014–2017).

5.1.2. Time Series 2015

The results below refer to a Sentinel-1 dataset from January 1st, 2015 to January 1st, 2016. During this period 55 images were captured over the AOI. Fig. 29 presents the chosen test site with coloration for frequency classes based on backscatter thresholds equaling –10 dB, –15 dB and –20 dB.

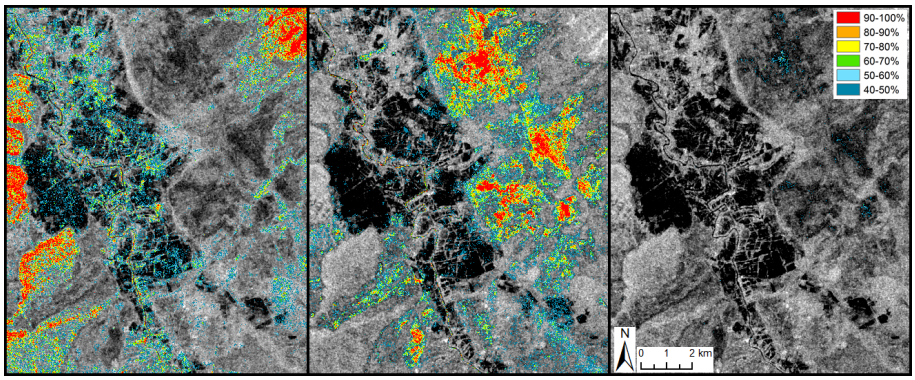

Fig. 29: Frequency classes in the study area in Somalia with τ equal to –10 dB, –15 dB and –20 dB (left to right) with the Sentinel-1 image as background (2015).

Frequency –10 dB

Table 7 summarizes results for the $\tau = -10$ dB threshold, which shows the parameter to be ineffective for the Somalia test site. The original image cannot be improved by any class, with only 90-100% (Result 7) able to match the accuracy values (Fig. 30). Detailed data are shown in Table 21 in Appendix B.

Table 7: Comparison of all accuracy results for $\tau = -10$ dB (2015)

		Result 1 (S-1FS)	Result 2 (40-100%)	Result 3 (50-100%)	Result 4 (60-100%)	Result 5 (70-100%)	Result 6 (80-100%)	Result 7 (90-100%)
OA		93.7	90.9	92.3	93.5	93.6	93.7	93.7
PA	Flood	96.3	75.6	85.7	94.3	95.5	96.0	96.2
	non Flood	93.3	93.5	93.4	93.3	93.3	93.3	93.3
UA	Flood	70.5	65.8	68.3	70.1	70.4	70.5	70.5
	non Flood	99.3	95.8	97.5	99.0	99.2	99.3	99.3

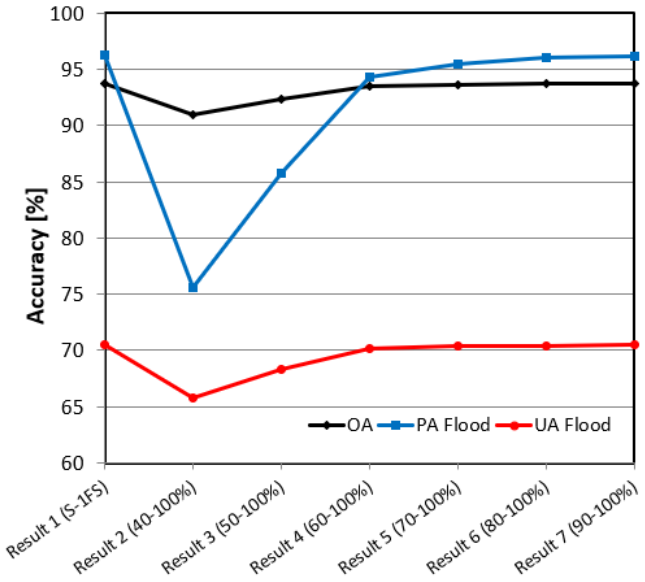

Fig. 30: Plot with accuracies of frequency classes with $\tau = -10$ dB (2015).

Frequency –15 dB

Similar to the years 2014–2017, the results displayed in Table 8 indicate that the threshold –15 dB, especially in the class range 60-100%, can improve S-1FS accuracy. To illustrate the results Fig. 31 is attached. PA in the original image is equal to 96.3%, and it insignificantly decreases to 95% (Result 4), but UA increases over 20.6% to 91.1%. OA accuracy is equal to 98.0%. Although OA has the same value in Result 3 (50-100%), the Producer's and User's Accuracy from Result 4 are slightly better. Detailed pixels statistics are given in Table 22 in Appendix B.

Table 8: Comparison of all accuracy results for $\tau = -15$ dB (2015)

		Result 1 (S-1FS)	Result 2 (40-100%)	Result 3 (50-100%)	Result 4 (60-100%)	Result 5 (70-100%)	Result 6 (80-100%)	Result 7 (90-100%)
OA		93.7	97.3	98.0	98.0	97.4	96.6	95.5
PA	Flood	96.3	85.5	91.1	95.0	95.5	95.8	96.0
	non Flood	93.3	99.3	99.1	98.5	97.8	96.8	95.5
UA	Flood	70.5	95.2	94.5	91.1	87.7	83.1	77.9
	non Flood	99.3	97.6	98.5	99.2	99.2	99.3	99.3

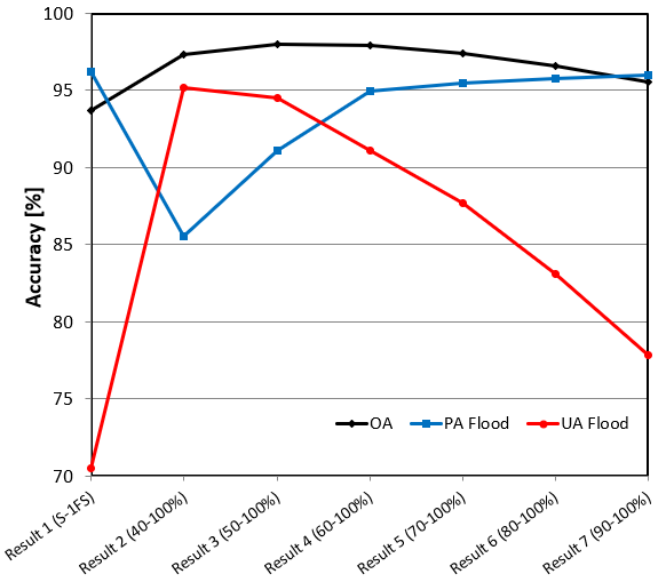

Fig. 31: Plot with accuracies of frequency classes with $\tau = -15$ dB (2015).

Frequency –20 dB

As can be seen in Table 9 and Fig. 32, parameter $\tau = -20$ dB does not influence results from the original image. Only Result 2 (40-100%) slightly improves the accuracy (see Table 23 in Appendix B), but it is not relevant statistically.

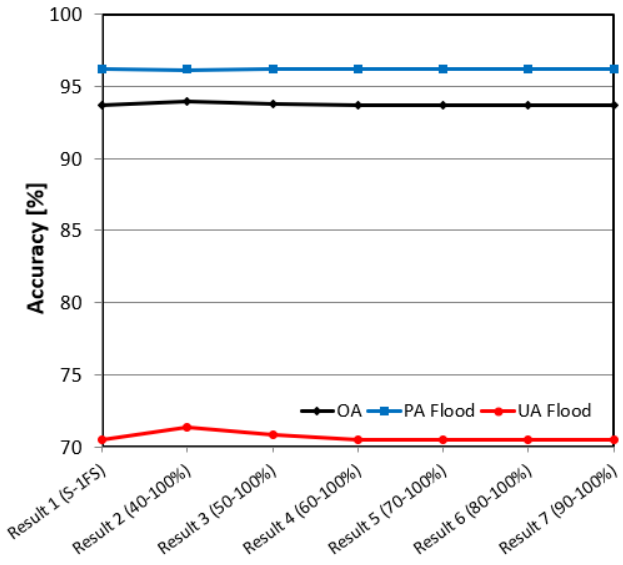

Fig. 32: Plot with accuracies of frequency classes with $\tau = -20$ dB (2015).

Table 9: Comparison of all accuracy results for $\tau = -20$ dB (2015)

		Result 1 (S-1FS)	Result 2 (40-100%)	Result 3 (50-100%)	Result 4 (60-100%)	Result 5 (70-100%)	Result 6 (80-100%)	Result 7 (90-100%)
OA		93.7	94.0	93.8	93.7	93.7	93.7	93.7
PA	Flood	96.3	96.2	96.2	96.2	96.3	96.3	96.3
	non Flood	93.3	93.6	93.4	93.3	93.3	93.3	93.3
UA	Flood	70.5	71.4	70.8	70.5	70.5	70.5	70.5
	non Flood	99.3	99.3	99.3	99.3	99.3	99.3	99.3

5.1.3. Time Series 2016

For time series data from the period January 1st, 2016 to January 1st, 2017, 64 images from the Sentinel-1 mission ware captured and merged by the Python-based tool into frequency maps with different thresholds. Below, in Fig. 33, maps with τ equal to –10 dB, -15 dB and –20 dB are presented.

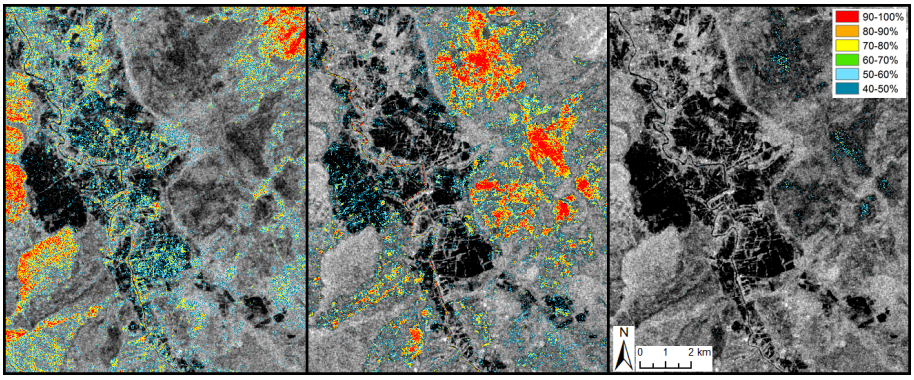

Fig. 33: Frequency classes in the study area in Somalia with τ equal to –10 dB, –15 dB and –20 dB (left to right) with the Sentinel-1 image as background (2016).

Frequency –10 dB

The results outlined in Table 10 show once again that $\tau = -10$ dB is not useful for accuracy improvement. No frequency class is able to improve the results

Table 10: Comparison of all accuracy results for $\tau = -10$ dB (2016)

		Result 1 (S-1FS)	Result 2 (40-100%)	Result 3 (50-100%)	Result 4 (60-100%)	Result 5 (70-100%)	Result 6 (80-100%)	Result 7 (90-100%)
OA		93.7	91.2	92.7	93.5	93.5	93.7	93.7
PA	Flood	96.3	77.5	89.0	94.4	94.4	96.0	96.2
	non Flood	93.3	93.4	93.4	93.3	93.3	93.3	93.3
UA	Flood	70.5	66.2	69.0	70.1	70.1	70.5	70.5
	non Flood	99.3	96.1	98.1	99.0	99.0	99.3	99.3

of S-1FS and similarly to the other years, only Result 7 (90-100% frequency class) is

able to reach the accuracies of the original image (Fig. 34). In Appendix B, Table 24 shows detailed calculations for all frequency ranges.

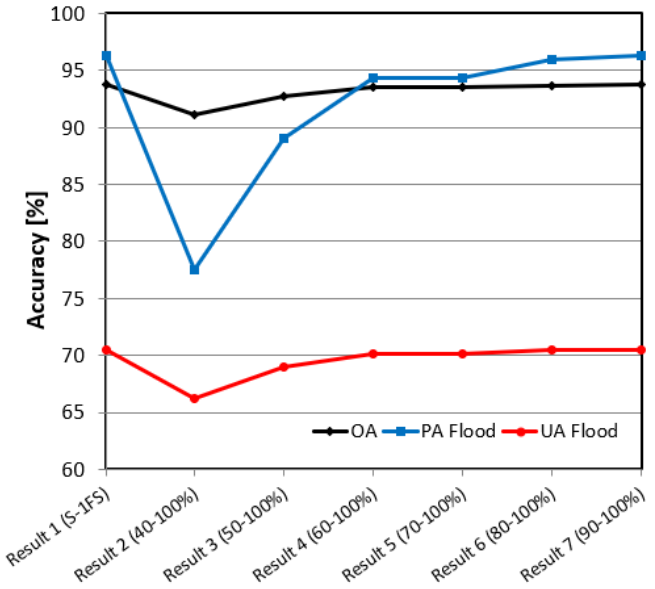

Fig. 34: Plot with accuracies of frequency classes with $\tau = -10$ dB (2016).

Frequency –15 dB

The analysis of the –15 dB backscatter threshold (Table 11) indicates that the highest accuracy improvement is achieved with Results 4 and 5. The OA improves by 4.2% up to 97.9%. Much like previous cases, the detection of ground truth flood pixels (or PA) decreases 3%, but looking at the 22% increase in UA for these results, it is clear that the percentage of pixels classified as flood which actually are flood is significantly improved (for visual representation, see Fig. 35, and for detailed statistics of frequency classes, refer to Table 25 in Appendix B).

Table 11: Comparison of all accuracy results for $\tau = -15$ dB (2016)

		Result 1 (S-1FS)	Result 2 (40-100%)	Result 3 (50-100%)	Result 4 (60-100%)	Result 5 (70-100%)	Result 6 (80-100%)	Result 7 (90-100%)
OA		93.7	96.5	97.7	97.9	97.9	97.5	96.2
PA	Flood	96.3	79.3	89.0	93.3	93.3	95.0	95.8
	non Flood	93.3	99.3	99.1	98.7	98.7	97.9	96.2
UA	Flood	70.5	95.1	94.3	92.4	92.4	88.3	80.8
	non Flood	99.3	96.7	98.2	98.9	98.9	99.2	99.3

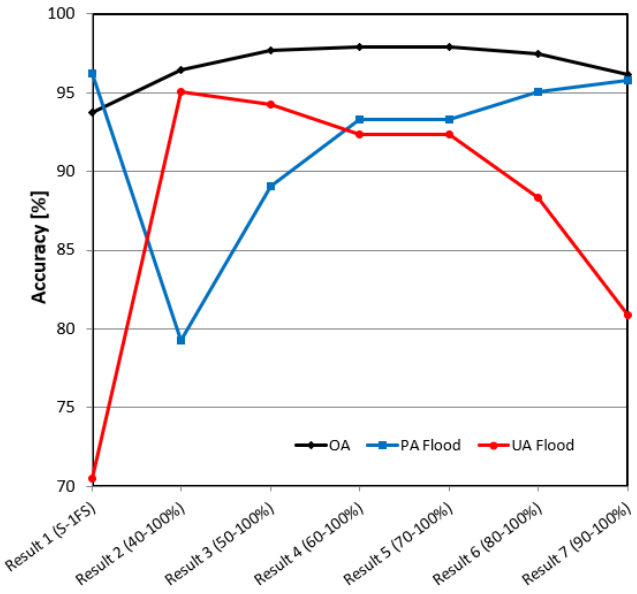

Fig. 35: Plot with accuracies of frequency classes with $\tau = -15$ dB (2016).

Frequency –20 dB

Table 12 displays accuracies for $\tau = -20$ dB. Result 2 shows the highest improvement possibilities, but they are not significant - OA increases only 0.5%, UA increases 1.6% and PA decreases 0.1% (Fig. 36). The detailed frequency calculations are attached to Appendix B in Table 26.

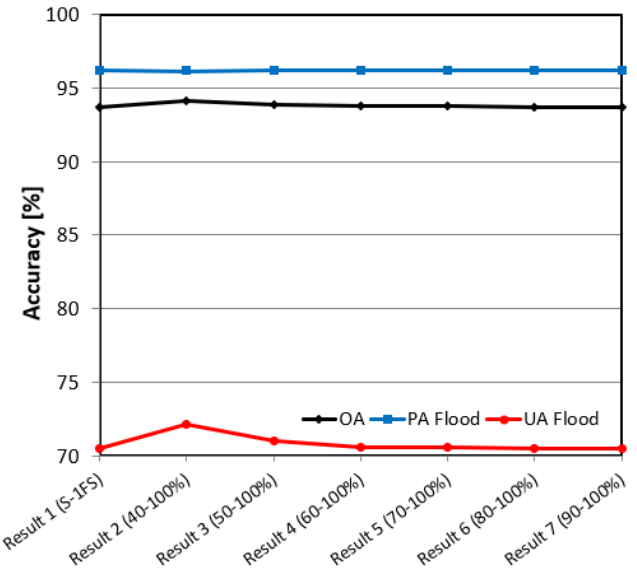

Fig. 36: Plot with accuracies of frequency classes with $\tau = -20$ dB (2016).

Table 12: Comparison of all accuracy results for $\tau = -20$ dB (2016)

		Result 1 (S-1FS)	Result 2 (40-100%)	Result 3 (50-100%)	Result 4 (60-100%)	Result 5 (70-100%)	Result 6 (80-100%)	Result 7 (90-100%)
OA		93.7	94.2	93.9	93.8	93.8	93.7	93.7
PA	Flood	96.3	96.2	96.2	96.2	96.2	96.2	96.3
	non Flood	93.3	93.8	93.5	93.3	93.3	93.3	93.3
UA	Flood	70.5	72.1	71.0	70.6	70.6	70.5	70.5
	non Flood	99.3	99.3	99.3	99.3	99.3	99.3	99.3

Summary

Based on the results described in previous subchapters, it can be said that using threshold $\tau = -15$ dB for an exclusion layer in the test site in Somalia gives the highest overall accuracy. Additionally, the best results are obtained using a frequency range of 60-100%, referring to pixels which were detected with backscatter value below threshold τ at least 60% of the time in time series analysis. Comparing the different time series durations used with the original S-1FS image (Fig. 37, Table 13) leads to the conclusion that each time series improves results, but 2014–2017 slightly more than others.

Table 13: Comparison of all accuracy results

		Result 1 (S-1FS)	Result 2 (2015)	Result 3 (2016)	Result 4 (2014-2017)
OA		93.7	98.0	97.9	98.4
PA Flood	Flood	96.3	95.0	93.3	93.7
	non Flood	93.3	98.5	98.7	99.1
UA Flood	Flood	70.5	91.1	92.4	94.7
	non Flood	99.3	99.2	98.9	99.0

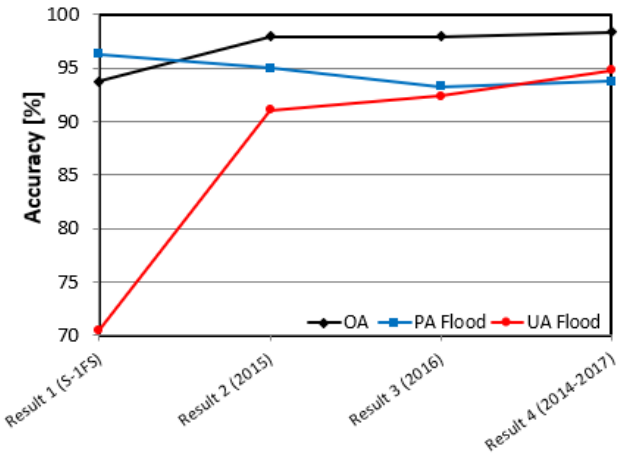

Fig. 37: Plot with accuracies of time series durations.

Fig. 38 illustrates the classification accuracy of threshold –15 dB (over the 2014–2017 time period) in which the color blue denotes areas where a flood occurred and which were correctly classified as inundated. White areas are the ones that are categorized as non-flood and in reality were not flooded. Green and red regions are falsely assigned - red being assigned to flood where in reality it was not flooded, and green as not flooded where it actually was an inundated region.

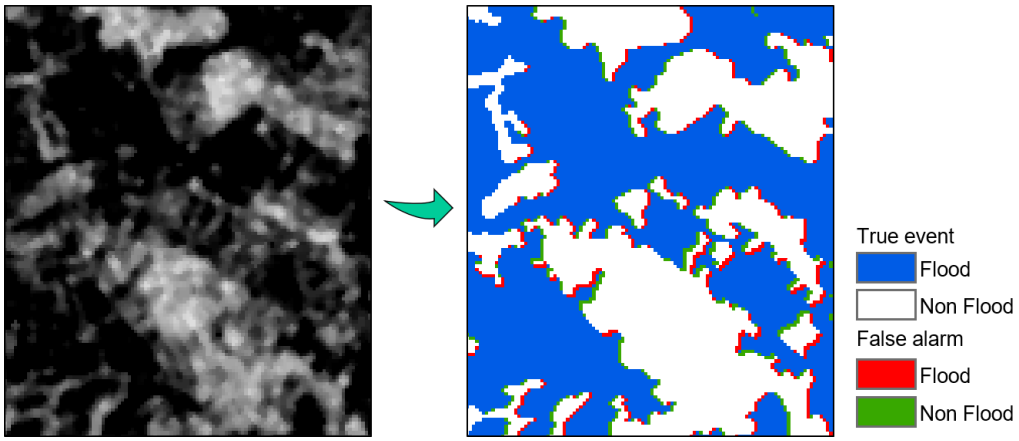

Fig. 38: Map with true events and false alarms.

5.1.4. Sentinel-1 Time Series vs MODIS

For comparison, the MODIS backscatter data is used for generation of an exclusion layer for improvement of S-1FS. The landcover class referred to as "Barren or sparsely vegetated" (Class 16) is used for the creation of a flood mask (Fig. 39). The results from original Sentinel-1 data and the highest accuracies from each time

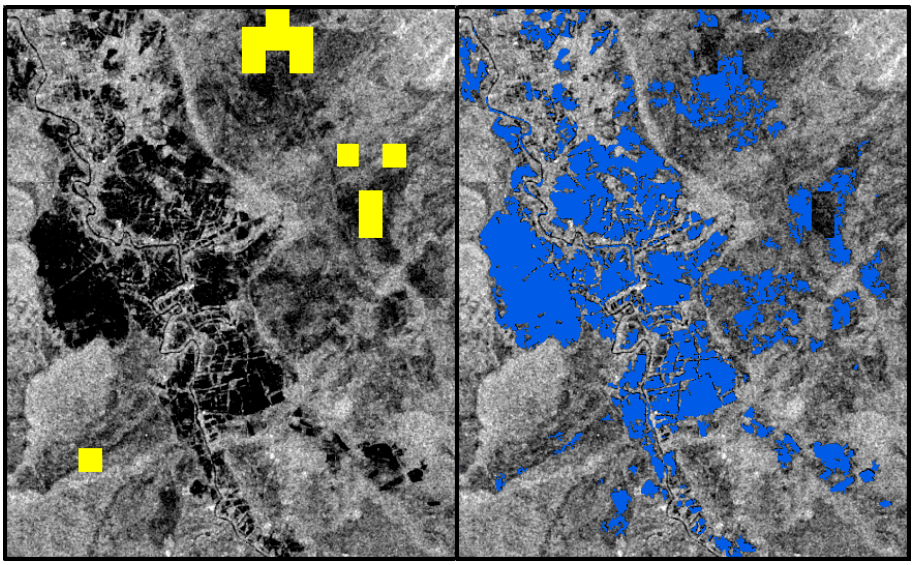

Fig. 39: MODIS Class 16 (on left) and MODIS-based improvement of S-1FS flood mask (on right).

series period are compared to MODIS (Table 14, Fig. 40). MODIS only slightly increases the User's Accuracy, by about 3%, but PA does not change. Clearly, the time series method discussed in this thesis reaches higher values in both User Accuracy and also Overall Accuracy.

Table 14: Comparison of time series accuracies with MODIS

		Result 1 (S-1FS)	Result 2 (MODIS)	Result 3 (2015)	Result 4 (2016)	Result 5 (2014-2017)
OA		93.7	94.5	98.0	97.9	98.4
PA Flood	Flood	96.3	96.3	95.0	93.3	93.7
	non Flood	93.3	94.2	98.5	98.7	99.1
UA Flood	Flood	70.5	73.4	91.1	92.4	94.7
	non Flood	99.3	99.3	99.2	98.9	99.0

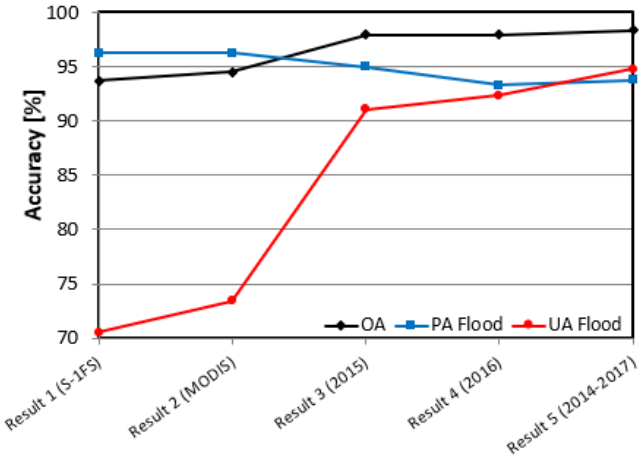

Fig. 40: Plot of accuracies of time series and MODIS.

5.2. Iraq

This subchapter helps to address the third research question. The flooding which occurred in October 2015 in Iraq was entirely in sandy regions, and, because of difficulties involving analysis of sand in SAR data, this event is a good example to test the limitations of this method.

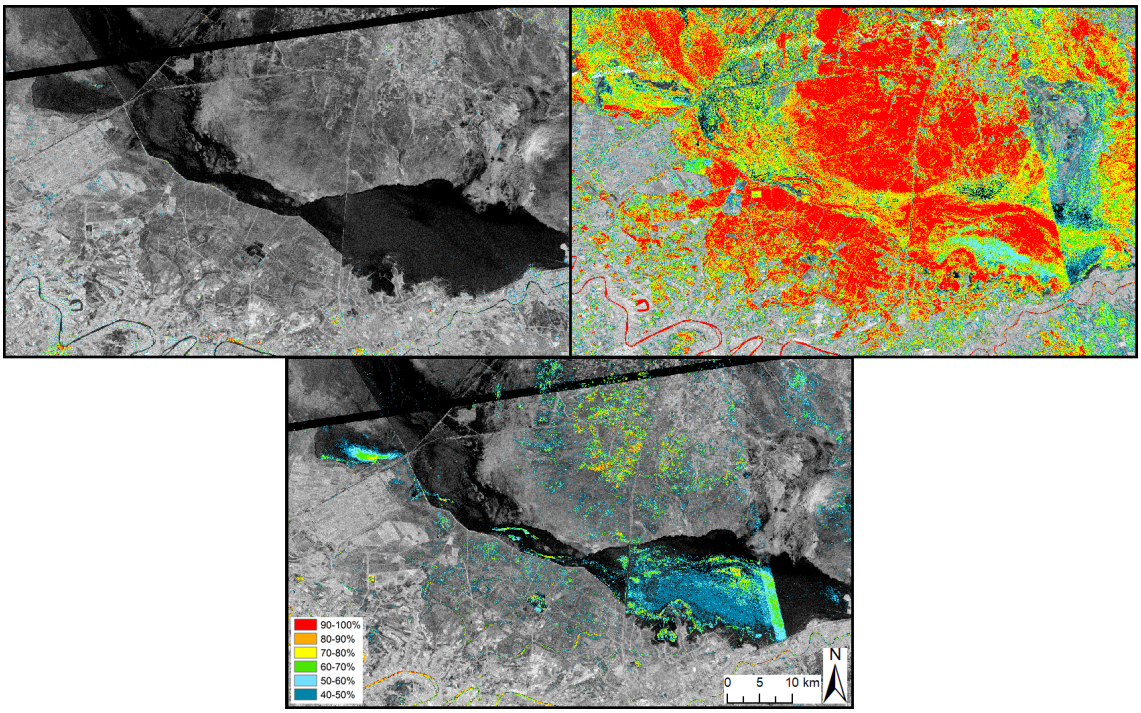

Fig. 41: Frequency classes in the study area in Iraq with τ equal –10 dB (top left), –15 dB (top right) and –20 dB (bottom) with the Sentinel-1 image as background.

The Area of Interest in Iraq is examined for one year of data spanning January

1st, 2016 to January 1st, 2017. The decision to limit the time series to one year was based on the Somalia tests, where the enhancement from using a three-year series was relatively insignificant, while involving higher computational demand. 79 images from Sentinel-1 were captured over the chosen AOI. Similar to Somalia, the tested backscatter thresholds are: –10 dB, –15 dB and –20 dB (Fig. 41).

Frequency –10 dB

Table 15 shows the results of tests performed using threshold –10 dB. It can be seen that there is no accuracy improvement from the tests, and that changes in classifications of the pixels in frequency classes are insignificant (see Table 27 in Appendix B). Visual confirmation can be found in Fig. 42. Thus the –10 dB threshold parameter does not seem to be useful for this region.

Table 15: Comparison of all accuracy results for $\tau = -10$ dB in Iraq

		Result 1 (S-1FS)	Result 2 (40-100%)	Result 3 (50-100%)	Result 4 (60-100%)	Result 5 (70-100%)	Result 6 (80-100%)	Result 7 (90-100%)
OA		87.0	87.0	87.0	87.0	87.0	87.0	87.0
PA	Flood	67.5	67.5	67.5	67.5	67.5	67.5	67.5
	non Flood	90.8	90.8	90.8	90.8	90.8	90.8	90.8
UA	Flood	58.6	58.6	58.6	58.6	58.6	58.6	58.6
	non Flood	93.5	93.5	93.5	93.5	93.5	93.5	93.5

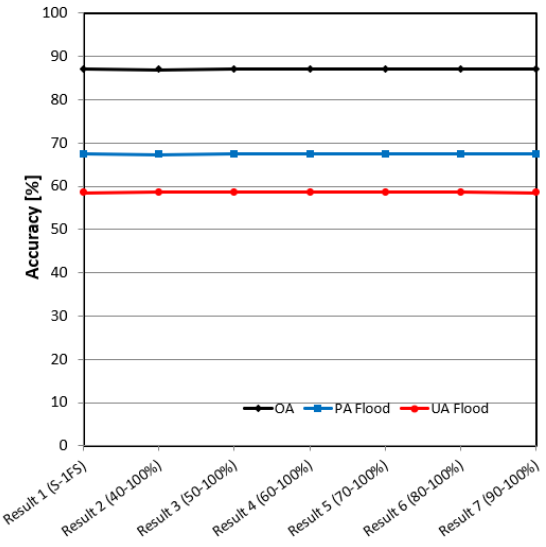

Fig. 42: Plot with accuracies of frequency classes with $\tau = -10$ dB in Iraq.

Frequency –15 dB

As can be seen in Fig. 41, the high-frequency classes for -15 dB cause most of the flooded area to be included in the exclusion layer. This negatively affects the Producer's Accuracy, which represents how many pixels from the ground truth flood were actually classified as a flood. Table 16 shows PA for the tests ranging from as low as 5.1% to 47.6% at best. Comparing those values to a PA of 67.5% in the original data suggests low usability of this parameter. In User's Accuracy, results show an increase in accuracy of between 3.9–7.2%, but Overall Accuracy has decreased, confirming the threshold –15 dB to be ineffective (see Fig. 43). The detailed statistical data are attached in Appendix B in Table 28.

Table 16: Comparison of all accuracy results for $\tau = -15$ dB in Iraq

		Result 1 (S-1FS)	Result 2 (40-100%)	Result 3 (50-100%)	Result 4 (60-100%)	Result 5 (70-100%)	Result 6 (80-100%)	Result 7 (90-100%)
OA		87.0	84.2	84.6	85.1	85.7	86.4	86.9
PA	Flood	67.5	5.1	9.8	16.9	24.6	36.5	47.6
	non Flood	90.8	99.4	99.0	98.3	97.5	96.0	94.5
UA	Flood	58.6	63.6	65.7	65.8	65.5	63.8	62.5
	non Flood	93.5	84.4	85.0	86.0	87.0	88.7	90.3

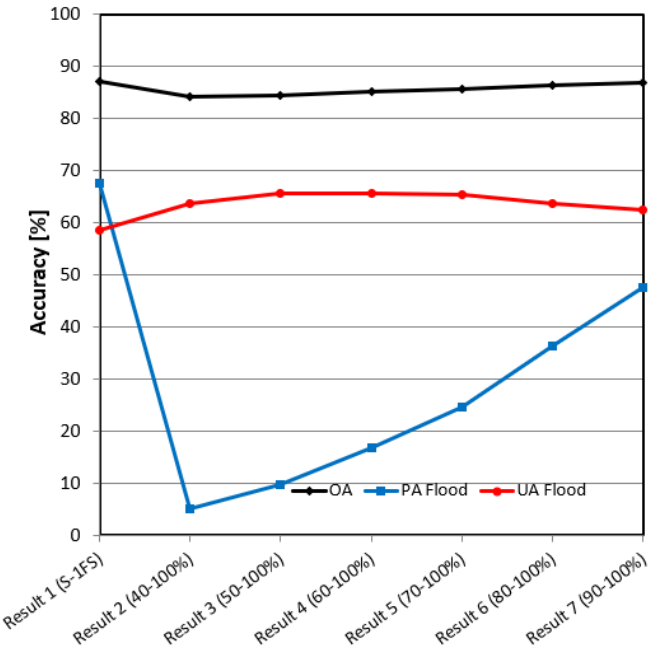

Fig. 43: Plot with accuracies of frequency classes with $\tau = -15$ dB in Iraq.

Frequency –20 dB

Table 17 displays the accuracy improvements generated by $\tau = -20$ dB. Result 6 offers a small improvement over the original S-1FS image. UA increases 0.6%, while PA drops from 67.5% to 67.3%, with the overall effect being 0.2% better OA. Fig. 44 illustrates those results (detailed confusion matrices are in Table 29 in Appendix B).

Table 17: Comparison of all accuracy results for $\tau = -20$ dB in Iraq

		Result 1 (S-1FS)	Result 2 (40-100%)	Result 3 (50-100%)	Result 4 (60-100%)	Result 5 (70-100%)	Result 6 (80-100%)	Result 7 (90-100%)
OA		87.0	86.2	86.7	87.1	87.2	87.2	87.1
PA	Flood	67.5	52.4	59.2	64.2	66.5	67.3	67.5
	non Flood	90.8	92.7	92.0	91.5	91.3	91.0	90.9
UA	Flood	58.6	58.0	58.9	59.4	59.5	59.2	58.8
	non Flood	93.5	91.0	92.1	93.0	93.4	93.5	93.5

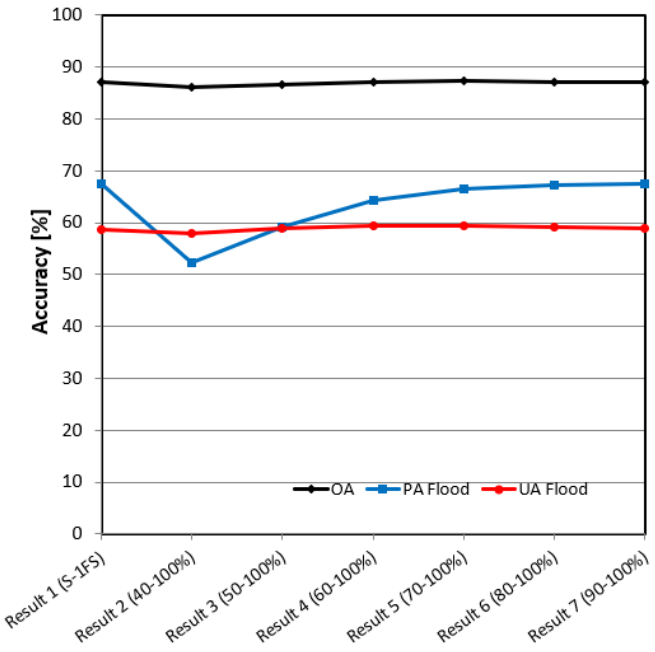

Fig. 44: Plot with accuracies of frequency classes with $\tau = -20$ dB in Iraq.

Summary

Table 18 present a comparison between the accuracy of the S-1FS image and the results obtained from tests using time series. Only threshold –20 dB (with the 80-100% frequency class) is able to improve accuracy, but just by 0.2% overall. Based on these results it can be concluded that this method has considerable limitations when the flood is occurring on areas permanently covered by sandy surfaces with low backscatter. In such situations, inundation of the terrain is not detected.

Table 18: Accuracies of time series durations in Iraq

		Result 1 (S-1FS)	Result 2 (-10)	Result 3 (-15)	Result 4 (-20)
OA		87.0	87.0	85.1	87.2
PA Flood	Flood	67.5	67.5	16.9	66.5
	non Flood	90.8	90.8	98.3	91.3
UA Flood	Flood	58.6	58.6	65.8	59.5
	non Flood	93.5	93.5	86.0	93.4

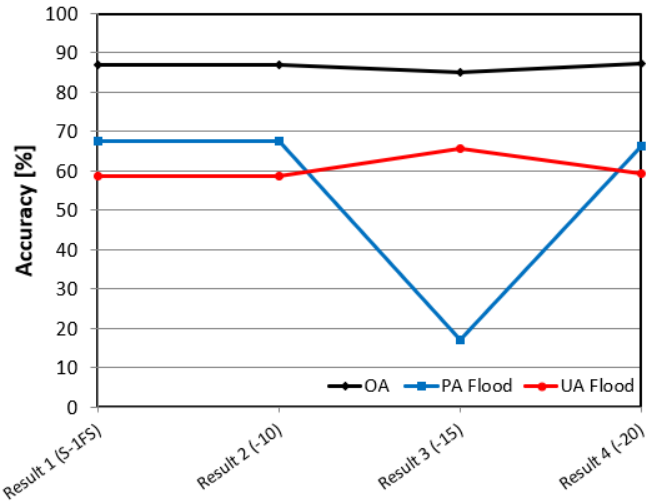

Fig. 45: Plot with accuracies of time series durations in Iraq.

6. Conclusions

This thesis tests Sentinel-1 time-series data for flood mapping in arid areas. The technique includes automatic Sentinel-1 data ingestion, geometric correction, radiometric calibration, computation, and merging of statistics layers. The proposed approach aims to improve the classification accuracy of automatic Sentinel-1 Flood Service. The service is designed for the detection of floods from a single SAR image. Particular attention is focused on arid regions in which one SAR dataset fails to differentiate water and other low backscatter regions.

6.1. Key Findings

This study was guided by three research questions. To answer the main question, the second and third questions will be addressed first.

Research question 2:
What is the influence of time-series parameters on classification accuracy?

From the outcome of experiments described in this thesis, it is possible to conclude that time-series parameters greatly influence the classification accuracy. An important implication of the performed tests is the significance of selecting a proper backscatter threshold and the frequency class for accuracy improvement. This study was also focused on the importance of time series duration. The results confirmed that a longer period of analysis leads to higher accuracy. It is important to have in mind the balance between accuracy improvement and computing time. A good example of that was the test in Somalia. Although a three-year time series had the highest accuracy, it was only 0.4% better than with a one-year period. The computation of time series data for 2014–2017 took five days, whereas both 2015 and 2016 needed less than a day to be processed. In this case clearly a one-year time series was viable choice, especially if the results have to be quickly distributed to disaster management authorities.

Research question 3:
What are the uncertainties and limitations of this approach?

The main limitation of this method is related to the surface on which the flood occurs. The time series comparison is based on an exclusion layer of regions with continuous low backscatter when not flooded, so if inundation develops on an

area permanently covered by sand, the algorithm is not able to detect it. This is confirmed in the tests conducted in the Iraq area of study.

Another limitation is on the technological side of the approach. The time series algorithm downloads and processes all of the Sentinel-1 datasets from the chosen period. Each of the images is high quality, with correspondingly large file size. To perform the time series analysis for Somalia in 2014–2017 (200 images) about 400 GB was used, and this test site has an area of only 105 km^2. This issue deserves particular consideration if:

- larger areas need to be analyzed,
- there is a need for a longer period of time series, and
- Sentinel-1 satellite flies over the AOI with high frequency.

Research question 1:
Does the use of the Sentinel-1 time-series data improving flood mapping in arid areas in comparison to existing approaches not based on the time series?

From the research that has been carried out, it is possible to conclude that Sentinel-1 time-series data can improve flood mapping in arid areas. Statistical parameters of backscatter time series were tested to establish which one will eliminate water-lookalikes with the highest accuracy. Examination of two areas of interest took place: a flood in Somalia in May 2016 and a flood in Niger in November 2015. In the Somalia case, the method removed most of the unwanted, overestimated regions through the application of the exclusion mask, ultimately showing very promising results with an Overall Accuracy of 98.4%, as well as a Producer's Accuracy value of 93.7% and User's Accuracy of 94.7%, the latter indicating an improvement of more than 24%. Those results were gained by using the 60–100% frequency classes for generation of the exclusion layer.

The originality of method presented in this thesis lies in the fact that a long period of time was used for analysis of interest areas. Using time series helps with detection of water-lookalikes. Confirmation of that can be found in the test carried out with MODIS data, which with its low coverage, led to only slight improvement of User's Accuracy, with a value of 3%.

6.2. Recommendations for Future Research

Until now, generation of exclusion layers consumes a substantial amount of time. In near-real-time flood mapping, fast response is one of the most important factors. Future work is needed to produce world-wide exclusion layers for arid areas. Implementation of this exclusion layer with the Sentinel-1 Flood Service would lead to higher classification accuracy with a short amount of computation time, critical for end users with time constraints for action. Further research is required for solving the issue of poor detection of flooded sandy regions. Additional experiments with the method outlined in this thesis on other test sites are recommended.

References

AFP (2015). Iraq flood. 10.08.2017. Retrieved [10.08.2017] from http://www.presstv.com/Detail/2015/11/06/436555/Iraq-flooding-Baghdad.

AMS (2017a). Glossary of Meteorology: Electromagnetic spectrum. Retrieved [24.09.2017] from http://glossary.ametsoc.org/wiki/Electromagnetic_spectrum.

AMS (2017b). Glossary of Meteorology: Flood. Retrieved [10.09.2017] from http://glossary.ametsoc.org/wiki/Flood.

AMS (2017c). Glossary of Meteorology: Radar Frequency Bands. Retrieved [25.09.2017] from http://glossary.ametsoc.org/wiki/Radar_frequency_bands.

Attema, E. (2005). Mission Requirements Document for the European Radar Observatory Sentinel-1: ES-RS-ESA-SY-0007.

Baumann, P. (1999). Flood analysis: 1993 Mississippi Flood. Retrieved [28.09.2017] from http://www.oneonta.edu/faculty/baumanpr/geosat2/Flood_Management/FLOOD_MANAGEMENT.htm.

Berz, G., Kron, W., Loster, T., Rauch, E., Schimetschek, J., Schmieder, J., Siebert, A., Smolka, A., and Wirtz, A. (2001). World Map of Natural Hazards - A Global View of the Distribution and Intensity of Significant Exposures. *Natural Hazards*, 23(2/3):443–465.

Brisco, B., Touzi, R., van der Sanden, J. J., Charbonneau, F., Pultz, T. J., and D'Iorio, M. (2008). Water Resource Applications with RADARSAT-2 – a Preview. *International Journal of Digital Earth*, 1(1):130–147.

Brivio, P. A., Colombo, R., Maggi, M., and Tomasoni, R. (2010). Integration of Remote Sensing Data and GIS for Accurate Mapping of Flooded Areas. *International Journal of Remote Sensing*, 23(3):429–441.

Campbell, J. B. and Wynne, R. H. (2011). *Introduction to Remote Sensing*. Guilford, New York and London, 5th ed. edition.

Central Bank of Somalia (2009). Central Bank of Somalia – Economy and Finance. Retrieved [24.08.2017] from http://www.somalbanca.org/economy-and-finance.html.

Chung, H. W., Liu, C. C., Cheng, I. F., Lee, Y. R., and Shieh, M. C. (2015). Rapid Response to a Typhoon-Induced Flood with an SAR-Derived Map of Inundated Areas: Case Study and Validation. *Remote Sensing*, 7(9):11954–11973.

Climate-Data (2017). Precipitation in Beledweyne. Retrieved [10.08.2017] from https://en.climate-data.org/location/900/.

De Groeve, T. (2010). Flood Monitoring and Mapping Using Passive Microwave Remote Sensing in Namibia. *Geomatics, Natural Hazards and Risk*, 1(1):19–35.

Deutsch, M. and Ruggles, F. (1974). Optical Data Processing and Projected Applications of the ERTS-1 Imagery Covering the 1973 Mississippi River Valley Floods. *Journal of the American Water Resources Association*, 10(5):1023–1039.

Deutscher Wetterdienst (2016). Klimatafel von Beled Weyne (Belet Uen) / Somalia: Baseline climate means (1961-1990) from stations all over the world. Retrieved [23.08.2017] from https://www.dwd.de/DWD/klima/beratung/ak/ak_632400_kt.pdf.

Dumitru, C. O., Cui, S., Faur, D., and Datcu, M. (2015). Data Analytics for Rapid Mapping: Case Study of a Flooding Event in Germany and the Tsunami in Japan Using Very High Resolution SAR Images. *IEEE Journal of Selected Topics in Applied Earth Observations and Remote Sensing*, 8(1):114–129.

EMS (2015). EMS User Guide: Ancillary Information. Retrieved [17.09.2017] from https://www.dwd.de/DWD/klima/beratung/ak/ak_632400_kt.pdf.

ESA (2012). Sentinel-1: ESA's Radar Observatory Mission for GMES Operational Services.

ESA (2013). Sentinel-1 User Handbook. Retrieved [11.06.2017] from https://sentinel.esa.int/.

ESA (2014a). Scattering. Retrieved [01.08.2017] from https://earth.esa.int/handbooks/asar/CNTR1-1-2.html.

ESA (2014b). Sentinel-1 Satellite. Retrieved [21.08.2017] from http://www.esa.int/Our_Activities/Observing_the_Earth/Copernicus/Gearing_up_for_a_new_era_in_Earth_observation.

ESA (2015a). Sentinel-2 Satellite. Retrieved [22.08.2017] from http://www.esa.int/Our_Activities/Observing_the_Earth/Copernicus/Sentinel-2/Calling_all_photographers.

ESA (2015b). Sentinel-2 User Handbook. Retrieved [22.08.2017] from https://sentinel.esa.int/.

European Parliament (2007). Directive 2007/60/EC of the European Parliament and of the Council of 23 October 2007 on the assessment and management of flood risks. Retrieved [10.09.2017] from http://rod.eionet.europa.eu/instruments/630.

FAO (2011). Country Pasture/Forage Resource Profiles: Iraq. Retrieved [10.08.2017] from http://www.fao.org/ag/agp/agpc/doc/counprof/iraq/iraq.html#3.

FAO-SWALIM (2017). Seasons of Somalia. Retrieved [24.08.2017] from http://www.faoswalim.org/water/climate-somalia.

Feyisa, G. L., Meilby, H., Fensholt, R., and Proud, S. R. (2014). Automated Water Extraction Index: A New Technique for Surface Water Mapping Using Landsat Imagery. *Remote Sensing of Environment*, 140:23–35.

FloodList (2017). FloodList. Retrieved [11.06.2017] from floodlist.com.

FLOODsite (2009). Types of Floods. Retrieved [11.06.2017] from http://www.floodsite.net/juniorfloodsite/html/en/student/thingstoknow/hydrology/floodtypes.html.

Frazier, P. S. and Page, K. J. (2000). Water Body Detection and Delineation with Landsat TM Data. *Photogrammetric Engineering & Remote Sensing*, 66(12):1461–1467.

Galantowicz, J. F. (2002). High-Resolution Flood Mapping from Low-Resolution Passive Microwave Data. In *IGARSS 2002*, pages 1499–1502. IEEE.

Gao, B.-C. (1996). NDWI—A Normalized Difference Water Index for Remote Sensing of Vegetation Liquid Water from Space. *Remote Sensing of Environment*, 58(3):257–266.

Giustarini, L., Hostache, R., Matgen, P., Schumann, G. J.-P., Bates, P. D., and Mason, D. C. (2013). A Change Detection Approach to Flood Mapping in Urban Areas Using TerraSAR-X. *IEEE Transactions on Geoscience and Remote Sensing*, 51(4):2417–2430.

Giustarini, L., Vernieuwe, H., Verwaeren, J., Chini, M., Hostache, R., Matgen, P., Verhoest, N., and de Baets, B. (2015). Accounting for Image Uncertainty in SAR-based Flood Mapping. *International Journal of Applied Earth Observation and Geoinformation*, 34:70–77.

Google Earth (2017). Satellite images. Retrieved [06.06.2017] from Google Earth.

Green, A. A., Whitehouse, G., and Outhet, D. (2007). Causes of Flood Streamlines Observed on Landsat Images and Their Use as Indicators of Floodways. *International Journal of Remote Sensing*, 4(1):5–16.

Henry, J.-B., Chastanet, P., Fellah, K., and Desnos, Y.-L. (2006). Envisat Multi–Polarized ASAR Data for Flood Mapping. *International Journal of Remote Sensing*, 27(10):1921–1929.

Herrera-Cruz, V. and Koudogbo, F. (2009). TerraSAR-X Rapid Mapping for Flood Events. In Heipke, C., Jacobsen, K., Müller, S., and Sörgel, U., editors, *ISPRS Hannover Workshop 2009*, volume WG VI/4.

Hong, Y., Adhikari, P., and Gourley, J. J. (2013). Flood Hazard and Disaster. In Bobrowsky, P. T., editor, *Encyclopedia of Natural Hazards*, Encyclopedia of Earth Sciences Series, pages 326–336. Springer Netherlands, Dordrecht.

Horritt, M. (2003). Waterline Mapping in Flooded Vegetation from Airborne SAR Imagery. *Remote Sensing of Environment*, 85(3):271–281.

Hung, M.-C. and Wu, Y.-H. (2005). Mapping and visualizing the Great Salt Lake landscape dynamics using multi–temporal satellite images, 1972–1996. *International Journal of Remote Sensing*, 26(9):1815–1834.

IEEE-AESS (2003). IEEE Standard for Letter Designations for Radar-Frequency Bands. Retrieved [21.08.2017] from http://ieeexplore.ieee.org/document/1160089/.

Iraqi Red Crescent Society (2015). Flood Destructions in Iraq. Retrieved [10.08.2017] from http://www.ifrc.org/en/what-we-do/where-we-work/middle-east-and-north-africa/Iraqi-Red-Crescent-Society/.

Irimescu, A., Stancalie, G., Craciunescu, V., Flueraru, C., and Anderson, E. (2009). The Use of Remote Sensing and Gis Techniques in Flood Monitoring and Damage Assessment: A Study Case in Romania. In Jones, J. A. A., Vardanian, T. G., and Hakopian, C., editors, *Threats to global water security*, NATO science for peace and security series. Series C, Environmental security, pages 167–177. Springer, Dordrecht and London.

Jain, S. K., Singh, R. D., Jain, M. K., and Lohani, A. K. (2005). Delineation of Flood-Prone Areas Using Remote Sensing Techniques. *Water Resources Management*, 19(4):333–347.

Jensen, J. R. (2007). *Remote Sensing of the Environment: An Earth Resource Perspective*. Prentice Hall series in geographic information science. Pearson Prentice Hall, Upper Saddle River, N.J., 2nd ed. edition.

Jiang, Z., Qi, J., Su, S., Zhang, Z., and Wu, J. (2012). Water Body Delineation using Index Composition and HIS Transformation. *International Journal of Remote Sensing*, 33(11):3402–3421.

Kiage, L. M., Walker, N. D., Balasubramanian, S., Babin, A., and Barras, J. (2005). Applications of Radarsat–1 Synthetic Aperture Radar Imagery to Assess Hurricane–Related Flooding of Coastal Louisiana. *International Journal of Remote Sensing*, 26(24):5359–5380.

Köppen, W. (1900). Versuch einer Klassifikation der Klimate, Vorzugsweise nach Ihren Beziehungen zur Pflanzenwelt: Attempted Climate Classification in Relation to Plant Distributions. *Geographische Zeitschrift*, 6(11):593–611.

Köppen, W. (1918). Klassifikation der Klimate nach Temperatur, Niederschlag und Jahresablauf: Classification of Climates According to Temperature, Precipitation and Seasonal Cycle. *Petermanns Geographische Mitteilungen*, 64:193–203.

Kottek, M., Grieser, J., Beck, C., Rudolf, B., and Rubel, F. (2006). World Map of the Köppen-Geiger climate classification updated. *Meteorologische Zeitschrift*, 15(3):259–263.

Kwak, Y., Arifuzzanman, B., and Iwami, Y. (2015). Prompt Proxy Mapping of Flood Damaged Rice Fields Using MODIS-Derived Indices. *Remote Sensing*, 7(12):15969–15988.

Li, J. and Narayanan, R. M. (2003). A Shape-Based Approach to Change Detection of Lakes Using Time Series Remote Sensing Images. *IEEE Transactions on Geoscience and Remote Sensing*, 41(11):2466–2477.

Lira, J. (2006). Segmentation and Morphology of Open Water Bodies from Multispectral Images. *International Journal of Remote Sensing*, 27(18):4015–4038.

Mallinis, G., Gitas, I. Z., Giannakopoulos, V., Maris, F., and Tsakiri-Strati, M. (2011). An Object-Based Approach for Flood Area Delineation in a Transboundary Area Using ENVISAT ASAR and LANDSAT TM Data. *International Journal of Digital Earth*, 24:1–13.

Marrion Consulting (2016). 4 Stages Disaster Management. Retrieved [19.08.2017] from http://www.marrionconsulting.com/services/fundamental-activities/disaster-management-planning/.

Martinis, S. (2017). Improving Flood Mapping in Arid Areas Using Sentinel-1 Time Series Data. In *IGARSS 2017*.

Martinis, S., Kersten, J., and Twele, A. (2015). A fully automated TerraSAR-X based flood service. *ISPRS Journal of Photogrammetry and Remote Sensing*, 104:203–212.

Martinis, S. and Twele, A. (2010). A Hierarchical Spatio-Temporal Markov Model for Improved Flood Mapping Using Multi-Temporal X-Band SAR Data. *Remote Sensing*, 2(9):2240–2258.

Martinis, S., Twele, A., and Voigt, S. (2009). Towards Operational Near Neal-Time Flood Detection Using a Split-based Automatic Thresholding Procedure on High Resolution TerraSAR-X Data. *Natural Hazards and Earth System Science*, 9(2):303–314.

Mason, D. C., Bates, P. D., and Dall'Amico, J. T. (2009). Calibration of Uncertain Flood Inundation Models Using Remotely Sensed Water Levels. *Journal of Hydrology*, 368(1-4):224–236.

Mason, D. C., Giustarini, L., Garcia-Pintado, J., and Cloke, H. L. (2014). Detection of Flooded Urban Areas in High Resolution Synthetic Aperture Radar Images Using Double Scattering. *International Journal of Applied Earth Observation and Geoinformation*, 28:150–159.

Matgen, P., Hostache, R., Schumann, G., Pfister, L., Hoffmann, L., and Savenije, H. (2011). Towards an Automated SAR-based Flood Monitoring System: Lessons Learned from Two Case Studies. *Physics and Chemistry of the Earth, Parts A/B/C*, 36(7-8):241–252.

McFeeters, S. K. (1996). The Use of the Normalized Difference Water Index (NDWI) in the Delineation of Open Water Features. *International Journal of Remote Sensing*, 17(7):1425–1432.

Moore, G. K. and North, G. W. (1974). Flood Inundation in the Southeastern United States from Aircraft and Satellite Imagery. *JAWRA Journal of the American Water Resources Association*, 10.

NASA (2014). Landsat 8 Satellite. Retrieved [22.08.2017] from https://www.nasa.gov/content/goddard/nasa-usgs-landsat-8-satellite-celebrates-first-year-of-success/.

National Governor's Association (1979). *State comprehensive emergency management: Final report of the Emergency Preparedness Project*. Defense Civil Preparedness Agency and Center for Policy Research, Washington, D.C., whittaker, hilary edition.

NHC (2003). Tropical Cyclone Report: Hurricane Lili, 21 September - 04 October 2002. Retrieved [01.10.2017] from http://www.nhc.noaa.gov/data/tcr/AL132002_Lili.pdf.

NSSL (2017). Severe Weather 101: Flood Types. Retrieved [11.09.2017] from http://www.nssl.noaa.gov/education/svrwx101/floods/types/.

OCHA/Linden (2015). Flood in Camp in Iraq, 2015. Retrieved [10.08.2017] from http://www.un.org/apps/news/story.asp.

Oliver, J. E. and Fairbridge, R. W. (1987). *The Encyclopedia of Climatology*, volume 11 of *Encyclopedia of Earth Sciences Series*. Van Nostrand Reinhold, New York.

Ouma, Y. O. and Tateishi, R. (2006). A Water Index for Rapid Mapping of Shoreline Changes of Five East African Rift Valley Lakes: An Empirical Analysis Using Landsat TM and ETM+ Data. *International Journal of Remote Sensing*, 27(15):3153–3181.

Peel, M. C., Finlayson, B. L., and McMahon, T. A. (2011). Updated World Map of the Köppen-Geiger Climate Classification. Desert Climate (BWh, BWk). Retrieved [11.06.2017] from https://en.wikipedia.org/wiki/Desert_climate.

Physics and Radio Electronics (2017). Active and passive sensors. Retrieved [10.06.2017] from http://www.physics-and-radio-electronics.com/blog/lidar-light-detection-ranging/.

Pulvirenti, L., Pierdicca, N., Chini, M., and Guerriero, L. (2011). An Algorithm for Operational Flood Mapping from Synthetic Aperture Radar (SAR) Data Using Fuzzy Logic. *Natural Hazards and Earth System Science*, 11(2):529–540.

Pulvirenti, L., Pierdicca, N., Chini, M., and Guerriero, L. (2013). Monitoring Flood Evolution in Vegetated Areas Using COSMO-SkyMed Data: The Tuscany 2009

Case Study. *IEEE Journal of Selected Topics in Applied Earth Observations and Remote Sensing*, 6(4):1807–1816.

Red Cross (2016). Flooded street in Beledweyne. Retrieved [25.08.2017] from http://somaliupdate.com/articles/8649/Somalia-30-000-People-Need-Food-Safe-Drinking-Water-After-Flooding.

Reliefweb (2015). Iraq Flood Watch. Retrieved [20.08.2017] from https://reliefweb.int/disaster/fl-2015-000153-irq.

Reliefweb (2017). Somalia Flood Watch. Retrieved [25.08.2017] from http://reliefweb.int/country/som.

Remund, J., Müller, S., Kunz, S., Huguenin-Landl, B., Studer, C., and Cattin, R. (2017). Meteonorm. Retrieved [10.08.2017] from https://weatherspark.com/y/103720/Average-Weather-in-Al-K%C5%ABt-Iraq-Year-Round.

Rogers, A. S. and Kearney, M. S. (2004). Reducing signature variability in unmixing coastal marsh Thematic Mapper scenes using spectral indices. *International Journal of Remote Sensing*, 25(12):2317–2335.

Salvia, M., Grings, F., Ferrazzoli, P., Barraza, V., Douna, V., Perna, P., Bruscantini, C., and Karszenbaum, H. (2011). Estimating flooded area and mean water level using active and passive microwaves: The example of Paraná River Delta floodplain. *Hydrology and Earth System Sciences*, 15(8):2679–2692.

Sapling Learning (2017). Electromagnetic spectrum. Retrieved [17.06.2017] from https://sites.google.com/site/chempendix/em-spectrum.

Schumann, G. (2015). Preface: Remote Sensing in Flood Monitoring and Management. *Remote Sensing*, 7(12):17013–17015.

Schumann, G. J.-P., Neal, J. C., Mason, D. C., and Bates, P. D. (2011). The Accuracy of Sequential Aerial Photography and SAR Data for Observing Urban Flood Dynamics, a Case Study of the UK Summer 2007 Floods. *Remote Sensing of Environment*, 115(10):2536–2546.

Scihub (2017). Sentinel-2 data. Retrieved [10.06.2017] from https://scihub.copernicus.eu/.

Sethre, P., Rundquist, B., and Todhunter, P. (2005). Remote Detection of Prairie Pothole Ponds in the Devils Lake Basin, North Dakota. *GIScience & Remote Sensing*, 42(4):277–296.

Sezgin, M. and Sankur, B. (2004). Survey over image thresholding techniques and quantitative performance evaluation. *Journal of Electronic Imaging*, 13(1):146.

Shabelle Foundation (2017). High level of Shabelle River. Retrieved [25.08.2017] from http://shabellefoundation.org/?p=129.

Sun, F., Sun, W., Chen, J., and Gong, P. (2012). Comparison and improvement of methods for identifying waterbodies in remotely sensed imagery. *International Journal of Remote Sensing*, 33(21):6854–6875.

SWALIM (2017). Flood monitoring. Retrieved [24.08.2017] from http://www.faoswalim.org/water/floods/flood-monitoring.

Tholey, N., Clandillon, S., and de Fraipont, P. (1997). The contribution of spaceborne SAR and optical data in monitoring flood events: Examples in northern and southern France. *Hydrological Processes*, 11(10):1409–1413.

Tralli, D. M., Blom, R. G., Zlotnicki, V., Donnellan, A., and Evans, D. L. (2005). Satellite remote sensing of earthquake, volcano, flood, landslide and coastal inundation hazards. *ISPRS Journal of Photogrammetry and Remote Sensing*, 59(4):185–198.

Twele, A., Cao, W., Plank, S., and Martinis, S. (2016). Sentinel-1-based Flood Mapping: A Fully Automated Processing Chain. *International Journal of Remote Sensing*, 37(13):2990–3004.

UNISDR, CRED (2016). Poverty & death: Disaster Mortality 1996-2015. Retrieved [17.08.2017] from http://www.preventionweb.net/publications/list/#hits=20&sortby=default&view=pw&filter=unisdrcontenttype%3A%5E%22Documents+%26+Publications%22%24%0D%0Ahazards%3A%5E%22Flood%22%2.

USGS (2016). Landsat 8 Data Users Handbook. Retrieved [22.08.2017] from https://landsat.usgs.gov/landsat-8-l8-data-users-handbook.

Wolff, C. (2017). Radar overlay. Retrieved [15.06.2017] from http://www.radartutorial.eu/20.airborne/ab07.en.html.

World Weather Online (2017). Temperatures in Beledweyne. Retrieved [10.09.2017] from https://www.worldweatheronline.com/beledweyne-weather-averages/hiiraan/so.aspx.

Wright, J. M. (2007). Floodplain management: Principles and current practices. Retrieved [11.08.2017] from https://training.fema.gov/hiedu/docs/fmc/chapter%202%20-%20types%20of%20floods%20and%20floodplains.pdf.

Xu, H. (2006). Modification of normalised difference water index (NDWI) to enhance open water features in remotely sensed imagery. *International Journal of Remote Sensing*, 27(14):3025–3033.

Appendices

Appendix A List of webpages

Database of charters activations - disastercharter.org
Emergency Events Database - emdat.be
Flood database - floodlist.com
Sentinel (1&2) data server - scihub.copernicus.eu
Landsat 8 data server - earthexplorer.usgs.gov

Appendix B Confusion matrices

Table 19: Confusion matrices for $\tau = -15$ dB (2014–2017)

Result 1 (Original mask)		Reference Data		Row total
		Flood	Non Flood	
Classification Data	Flood	142921	59806	202727
	Non Flood	5568	833255	838823
Column total		148489	893061	**1041550**

Result 5 (70-100%)		Reference Data		Row total
		Flood	Non Flood	
Classification Data	Flood	141135	10480	151615
	Non Flood	7354	882581	889935
Column total		148489	893061	**1041550**

Result 2 (40-100%)		Reference Data		Row total
		Flood	Non Flood	
Classification Data	Flood	125968	5528	131496
	Non Flood	22521	887533	910054
Column total		148489	893061	**1041550**

Result 6 (80-100%)		Reference Data		Row total
		Flood	Non Flood	
Classification Data	Flood	141875	15080	156955
	Non Flood	6614	877981	884595
Column total		148489	893061	**1041550**

Result 3 (50-100%)		Reference Data		Row total
		Flood	Non Flood	
Classification Data	Flood	134080	6312	140392
	Non Flood	14409	886749	901158
Column total		148489	893061	**1041550**

Results 7 (90-100%)		Reference Data		Row total
		Flood	Non Flood	
Classification Data	Flood	142499	31413	173912
	Non Flood	5990	861648	867638
Column total		148489	893061	**1041550**

Result 4 (60-100%)		Reference Data		Row total
		Flood	Non Flood	
Classification Data	Flood	139205	7720	146925
	Non Flood	9284	885341	894625
Column total		148489	893061	**1041550**

Table 20: Confusion matrices for $\tau = -20$ dB (2014–2017)

Result 1 (Original mask)		Reference Data		Row total
		Flood	Non Flood	
Classification Data	Flood	142921	59806	202727
	Non Flood	5568	833255	838823
Column total		148489	893061	**1041550**

Result 5 (70-100%)		Reference Data		Row total
		Flood	Non Flood	
Classification Data	Flood	142921	59806	202727
	Non Flood	5568	833255	838823
Column total		148489	893061	**1041550**

Result 2 (40-100%)		Reference Data		Row total
		Flood	Non Flood	
Classification Data	Flood	142901	56026	198927
	Non Flood	5588	837035	842623
Column total		148489	893061	**1041550**

Result 6 (80-100%)		Reference Data		Row total
		Flood	Non Flood	
Classification Data	Flood	142921	59806	202727
	Non Flood	5568	833255	838823
Column total		148489	893061	**1041550**

Result 3 (50-100%)		Reference Data		Row total
		Flood	Non Flood	
Classification Data	Flood	142921	58667	201588
	Non Flood	5568	834394	839962
Column total		148489	893061	**1041550**

Result 7 (90-100%)		Reference Data		Row total
		Flood	Non Flood	
Classification Data	Flood	142921	59806	202727
	Non Flood	5568	833255	838823
Column total		148489	893061	**1041550**

Result 4 (60-100%)		Reference Data		Row total
		Flood	Non Flood	
Classification Data	Flood	142921	59704	202625
	Non Flood	5568	833357	838925
Column total		148489	893061	**1041550**

Table 21: Confusion matrices for $\tau = -10$ dB (2015)

Result 1 (Original mask)		Reference Data		Row total
		Flood	Non Flood	
Classification Data	Flood	142921	59806	202727
	Non Flood	5568	833255	838823
Column total		148489	893061	**1041550**

Result 5 (70-100%)		Reference Data		Row total
		Flood	Non Flood	
Classification Data	Flood	141799	59720	201519
	Non Flood	6690	833341	840031
Column total		148489	893061	**1041550**

Result 2 (40-100%)		Reference Data		Row total
		Flood	Non Flood	
Classification Data	Flood	112227	58391	170618
	Non Flood	36262	834670	870932
Column total		148489	893061	**1041550**

Result 6 (80-100%)		Reference Data		Row total
		Flood	Non Flood	
Classification Data	Flood	142588	59781	202369
	Non Flood	5901	833280	839181
Column total		148489	893061	**1041550**

Result 3 (50-100%)		Reference Data		Row total
		Flood	Non Flood	
Classification Data	Flood	127284	58992	186276
	Non Flood	21205	834069	855274
Column total		148489	893061	**1041550**

Result 7 (90-100%)		Reference Data		Row total
		Flood	Non Flood	
Classification Data	Flood	142838	59799	202637
	Non Flood	5651	833262	838913
Column total		148489	893061	**1041550**

Result 4 (60-100%)		Reference Data		Row total
		Flood	Non Flood	
Classification Data	Flood	139988	59612	199600
	Non Flood	8501	833449	841950
Column total		148489	893061	**1041550**

Table 22: Confusion matrices for $\tau = -15$ dB (2015)

Result 1 (Original mask)		Reference Data		Row total
		Flood	Non Flood	
Classification Data	Flood	142921	59806	202727
	Non Flood	5568	833255	838823
Column total		148489	893061	**1041550**

Result 5 (70-100%)		Reference Data		Row total
		Flood	Non Flood	
Classification Data	Flood	141789	19956	161745
	Non Flood	6700	873105	879805
Column total		148489	893061	**1041550**

Result 2 (40-100%)		Reference Data		Row total
		Flood	Non Flood	
Classification Data	Flood	126990	6428	133418
	Non Flood	21499	886633	908132
Column total		148489	893061	**1041550**

Result 6 (80-100%)		Reference Data		Row total
		Flood	Non Flood	
Classification Data	Flood	142223	28970	171193
	Non Flood	6266	864091	870357
Column total		148489	893061	**1041550**

Result 3 (50-100%)		Reference Data		Row total
		Flood	Non Flood	
Classification Data	Flood	135255	7898	143153
	Non Flood	13234	885163	898397
Column total		148489	893061	**1041550**

Result 7 (90-100%)		Reference Data		Row total
		Flood	Non Flood	
Classification Data	Flood	142558	40548	183106
	Non Flood	5931	852513	858444
Column total		148489	893061	**1041550**

Result 4 (60-100%)		Reference Data		Row total
		Flood	Non Flood	
Classification Data	Flood	141004	13811	154815
	Non Flood	7485	879250	886735
Column total		148489	893061	**1041550**

Table 23: Confusion matrices for $\tau = -20$ dB (2015)

Result 1 (Original mask)		Reference Data		Row total
		Flood	Non Flood	
Classification Data	Flood	142921	59806	202727
	Non Flood	5568	833255	838823
Column total		148489	893061	**1041550**

Result 5 (70-100%)		Reference Data		Row total
		Flood	Non Flood	
Classification Data	Flood	142921	59795	202716
	Non Flood	5568	833266	838834
Column total		148489	893061	**1041550**

Result 2 (40-100%)		Reference Data		Row total
		Flood	Non Flood	
Classification Data	Flood	142889	57370	200259
	Non Flood	5600	835691	841291
Column total		148489	893061	**1041550**

Result 6 (80-100%)		Reference Data		Row total
		Flood	Non Flood	
Classification Data	Flood	142921	59806	202727
	Non Flood	5568	833255	838823
Column total		148489	893061	**1041550**

Result 3 (50-100%)		Reference Data		Row total
		Flood	Non Flood	
Classification Data	Flood	142914	58960	201874
	Non Flood	5575	834101	839676
Column total		148489	893061	**1041550**

Result 7 (90-100%)		Reference Data		Row total
		Flood	Non Flood	
Classification Data	Flood	142921	59806	202727
	Non Flood	5568	833255	838823
Column total		148489	893061	**1041550**

Result 4 (60-100%)		Reference Data		Row total
		Flood	Non Flood	
Classification Data	Flood	142920	59748	202668
	Non Flood	5569	833313	838882
Column total		148489	893061	**1041550**

Table 24: Confusion matrices for $\tau = -10$ dB (2016)

Result 1 (Original mask)		Reference Data		Row total
		Flood	Non Flood	
Classification Data	Flood	142921	59806	202727
	Non Flood	5568	833255	838823
Column total		148489	893061	**1041550**

Result 5 (70-100%)		Reference Data		Row total
		Flood	Non Flood	
Classification Data	Flood	140122	59644	199766
	Non Flood	8367	833417	841784
Column total		148489	893061	**1041550**

Result 2 (40-100%)		Reference Data		Row total
		Flood	Non Flood	
Classification Data	Flood	115018	58624	173642
	Non Flood	33471	834437	867908
Column total		148489	893061	**1041550**

Result 6 (80-100%)		Reference Data		Row total
		Flood	Non Flood	
Classification Data	Flood	142539	59776	202315
	Non Flood	5950	833285	839235
Column total		148489	893061	**1041550**

Result 3 (50-100%)		Reference Data		Row total
		Flood	Non Flood	
Classification Data	Flood	132147	59310	191457
	Non Flood	16342	833751	850093
Column total		148489	893061	**1041550**

Result 7 (90-100%)		Reference Data		Row total
		Flood	Non Flood	
Classification Data	Flood	142920	59806	202726
	Non Flood	5569	833255	838824
Column total		148489	893061	**1041550**

Result 4 (60-100%)		Reference Data		Row total
		Flood	Non Flood	
Classification Data	Flood	140122	59644	199766
	Non Flood	8367	833417	841784
Column total		148489	893061	**1041550**

Table 25: Confusion matrices for $\tau = -15$ dB (2016)

Result 1 (Original mask)		Reference Data		Row total
		Flood	Non Flood	
Classification Data	Flood	142921	59806	202727
	Non Flood	5568	833255	838823
Column total		148489	893061	**1041550**

Result 5 (70-100%)		Reference Data		Row total
		Flood	Non Flood	
Classification Data	Flood	138501	11441	149942
	Non Flood	9988	881620	891608
Column total		148489	893061	**1041550**

Result 2 (40-100%)		Reference Data		Row total
		Flood	Non Flood	
Classification Data	Flood	117750	6101	123851
	Non Flood	30739	886960	917699
Column total		148489	893061	**1041550**

Result 6 (80-100%)		Reference Data		Row total
		Flood	Non Flood	
Classification Data	Flood	141128	18630	159758
	Non Flood	7361	874431	881792
Column total		148489	893061	**1041550**

Result 3 (50-100%)		Reference Data		Row total
		Flood	Non Flood	
Classification Data	Flood	132202	8058	140260
	Non Flood	16287	885003	901290
Column total		148489	893061	**1041550**

Result 7 (90-100%)		Reference Data		Row total
		Flood	Non Flood	
Classification Data	Flood	142273	33714	175987
	Non Flood	6216	859347	865563
Column total		148489	893061	**1041550**

Result 4 (60-100%)		Reference Data		Row total
		Flood	Non Flood	
Classification Data	Flood	138501	11441	149942
	Non Flood	9988	881620	891608
Column total		148489	893061	**1041550**

Table 26: Confusion matrices for $\tau = -20$ dB (2016)

Result 1 (Original mask)		Reference Data		Row total
		Flood	Non Flood	
Classification Data	Flood	142921	59806	202727
	Non Flood	5568	833255	838823
Column total		148489	893061	**1041550**

Result 5 (70-100%)		Reference Data		Row total
		Flood	Non Flood	
Classification Data	Flood	142914	59481	202395
	Non Flood	5575	833580	839155
Column total		148489	893061	**1041550**

Result 2 (40-100%)		Reference Data		Row total
		Flood	Non Flood	
Classification Data	Flood	142820	55235	198055
	Non Flood	5669	837826	843495
Column total		148489	893061	**1041550**

Result 6 (80-100%)		Reference Data		Row total
		Flood	Non Flood	
Classification Data	Flood	142920	59768	202688
	Non Flood	5569	833293	838862
Column total		148489	893061	**1041550**

Result 3 (50-100%)		Reference Data		Row total
		Flood	Non Flood	
Classification Data	Flood	142889	58399	201288
	Non Flood	5600	834662	840262
Column total		148489	893061	**1041550**

Result 7 (90-100%)		Reference Data		Row total
		Flood	Non Flood	
Classification Data	Flood	142921	59804	202725
	Non Flood	5568	833257	838825
Column total		148489	893061	**1041550**

Result 4 (60-100%)		Reference Data		Row total
		Flood	Non Flood	
Classification Data	Flood	142914	59481	202395
	Non Flood	5575	833580	839155
Column total		148489	893061	**1041550**

Table 27: Confusion matrices for $\tau = -10$ dB in Iraq

Result 1 (Originalmaske)		Reference Data		Row total
		Flood	Non Flood	
Classification Data	Flood	4345106	3066738	7411844
	Non Flood	2088185	30231752	32319937
Column total		6433291	33298490	**39731781**

Classification 5 (70-100%)		Reference Data		Row total
		Flood	Non Flood	
Classification Data	Flood	4345097	3066541	7411638
	Non Flood	2088194	30231949	32320143
Column total		6433291	33298490	**39731781**

Result 2 (40-100%)		Reference Data		Row total
		Flood	Non Flood	
Classification Data	Flood	4340244	3063177	7403421
	Non Flood	2093047	30235313	32328360
Column total		6433291	33298490	**39731781**

Classification 6 (80-100%)		Reference Data		Row total
		Flood	Non Flood	
Classification Data	Flood	4345106	3066734	7411840
	Non Flood	2088185	30231756	32319941
Column total		6433291	33298490	**39731781**

Classification 3 (50-100%)		Reference Data		Row total
		Flood	Non Flood	
Classification Data	Flood	4344310	3064733	7409043
	Non Flood	2088981	30233757	32322738
Column total		6433291	33298490	**39731781**

Classification 7 (90-100%)		Reference Data		Row total
		Flood	Non Flood	
Classification Data	Flood	4345106	3066738	7411844
	Non Flood	2088185	30231752	32319937
Column total		6433291	33298490	**39731781**

Classification 4 (60-100%)		Reference Data		Row total
		Flood	Non Flood	
Classification Data	Flood	4344989	3066094	7411083
	Non Flood	2088302	30232396	32320698
Column total		6433291	33298490	**39731781**

Table 28: Confusion matrices for $\tau = -15$ dB in Iraq

Result 1 (Originalmaske)		Reference Data		Row total
		Flood	Non Flood	
Classification Data	Flood	4345106	3066738	7411844
	Non Flood	2088185	30231752	32319937
Column total		6433291	33298490	**39731781**

Classification 5 (70-100%)		Reference Data		Row total
		Flood	Non Flood	
Classification Data	Flood	1585337	835059	2420396
	Non Flood	4847954	32463431	37311385
Column total		6433291	33298490	**39731781**

Result 2 (40-100%)		Reference Data		Row total
		Flood	Non Flood	
Classification Data	Flood	329543	188672	518215
	Non Flood	6103748	33109818	39213566
Column total		6433291	33298490	**39731781**

Classification 6 (80-100%)		Reference Data		Row total
		Flood	Non Flood	
Classification Data	Flood	2345555	1331387	3676942
	Non Flood	4087736	31967103	36054839
Column total		6433291	33298490	**39731781**

Classification 3 (50-100%)		Reference Data		Row total
		Flood	Non Flood	
Classification Data	Flood	631370	329877	961247
	Non Flood	5801921	32968613	38770534
Column total		6433291	33298490	**39731781**

Classification 7 (90-100%)		Reference Data		Row total
		Flood	Non Flood	
Classification Data	Flood	3063176	1838362	4901538
	Non Flood	3370115	31460128	34830243
Column total		6433291	33298490	**39731781**

Classification 4 (60-100%)		Reference Data		Row total
		Flood	Non Flood	
Classification Data	Flood	1089476	566839	1656315
	Non Flood	5343815	32731651	38075466
Column total		6433291	33298490	**39731781**

Table 29: Confusion matrices for $\tau = -20$ dB in Iraq

Result 1 (Originalmaske)		Reference Data		Row total
		Flood	Non Flood	
Classification Data	Flood	4345106	3066738	7411844
	Non Flood	2088185	30231752	32319937
Column total		6433291	33298490	**39731781**

Classification 5 (70-100%)		Reference Data		Row total
		Flood	Non Flood	
Classification Data	Flood	4275323	2911742	7187065
	Non Flood	2157968	30386748	32544716
Column total		6433291	33298490	**39731781**

Result 2 (40-100%)		Reference Data		Row total
		Flood	Non Flood	
Classification Data	Flood	3370066	2437389	5807455
	Non Flood	3063225	30861101	33924326
Column total		6433291	33298490	**39731781**

Classification 6 (80-100%)		Reference Data		Row total
		Flood	Non Flood	
Classification Data	Flood	4332067	2991608	7323675
	Non Flood	2101224	30306882	32408106
Column total		6433291	33298490	**39731781**

Classification 3 (50-100%)		Reference Data		Row total
		Flood	Non Flood	
Classification Data	Flood	3811580	2663905	6475485
	Non Flood	2621711	30634585	33256296
Column total		6433291	33298490	**39731781**

Classification 7 (90-100%)		Reference Data		Row total
		Flood	Non Flood	
Classification Data	Flood	4343834	3041242	7385076
	Non Flood	2089457	30257248	32346705
Column total		6433291	33298490	**39731781**

Classification 4 (60-100%)		Reference Data		Row total
		Flood	Non Flood	
Classification Data	Flood	4129336	2826590	6955926
	Non Flood	2303955	30471900	32775855
Column total		6433291	33298490	**39731781**